Interaction of Graphene Quantum Dots with Oligothiophene: A Comprehensive Theoretical Study

Ayesha Ashraf,[†,‡] Kevin Carter-Fenk,[‡] John M. Herbert,[‡] Bilal Ahmad Farooqi,[†] Umar Farooq,[†] and Khurshid Ayub*,[§]

[†]Institute of Chemistry, University of the Punjab, Quaid-e-Azam Campus, Lahore 54590, Pakistan

[‡]Department of Chemistry and Biochemistry, The Ohio State University, Columbus, Ohio 43210, United States

[§]Department of Chemistry, COMSATS University Islamabad, Abbottabad Campus, Abbottabad 22060, Pakistan

S *Supporting Information*

ABSTRACT: Graphene/polythiophene composites are widely used in a variety of optoelectronic devices and applications, e.g., as electrode materials in capacitors and solar cells, but the detailed molecular-level relationship between their structural and electronic properties is not well understood. We present a density functional theory study of these composites using model systems consisting of graphene nanosheets and nanoribbons sandwiched between oligothiophenes (up to 13 monomers in length). These systems are investigated by computing optical band gaps, UV−visible spectra, densities of states, and by analyzing noncovalent interactions in terms of the reduced density gradient. Frontier molecular orbital analysis reveals a significant decrease in the optical band gap upon increasing the concentration of graphene, which can be tuned by adjusting the proportion of graphene using larger nanoribbons. This finding has implications for device design in these materials.
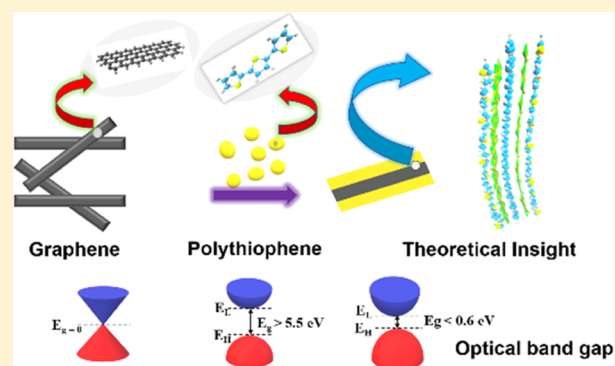
1. INTRODUCTION

The two-dimensional (2D) single-atom-thick sheet of sp^2-hybridized carbon atoms arranged in a honeycomb lattice in graphene makes it a more promising and captivating material for a large number of applications in nanoelectronics,[1] energy storage devices,[2] sensors,[3] drug delivery,[4] catalysis,[5] and quantum physics.[6] The pristine graphene has zero band gap, which limits its applications in the fields of sensors and semiconductors.[7] The electrical properties can be changed by tuning the band gap when different covalent and noncovalent functionalization approaches are used.[8] Chemical modification of graphene surface, reaction with inorganic and organic molecules, and taking into account different noncovalent and covalent interactions with graphene are some strategies for functionalization of graphene.[9−11] Intercalation, doping, striping techniques, cutting the graphene sheet into narrow ribbons, and applying external electric field to graphene bilayer are a few techniques to open the band gap of graphene for successful applications in nanoelectronics devices. Graphene can be easily processed into different morphological nanostructures, including ultrathin films,[12,13] nanosheets,[14−16] paper,[17] nanoribbons,[18,19] foams,[20,21] tetragonal graphene system,[22] and colloidal graphene quantum dots.[23] The tetragonal graphene sheet and nanoribbon system is often used as a model to compute optical properties and magnetic flux-induced electronic band tuning.[24] The incorporation of

graphene sheets with other functional moieties is an efficient route to improve its performance in diverse applications.[25] Graphene quantum dots possess unique electronic, photoluminescence, and electrochemical sensor properties.[26] Graphene quantum dots in diamond shape with different sizes are used to study their magnetic and optical properties with the help of density functional theory (DFT)[27] methods. Covalent modifications can improve the electronic properties of graphene, and this can be attained by chemically absorbing the molecules on graphene surface. This modification results in stable structures, but it alters the hybridization of graphene's carbon from sp^2 to sp^3 and leads to undesirable irreversible changes or sometimes exploitation of its electronic properties.[28]

The noncovalent approach takes advantage of dispersion interactions between adsorbate and graphene, and thus the carbon lattice does not suffer from undesirable and irreversible changes. The desired electronic properties of graphene are retained. The intrinsic properties of graphene are conserved by using noncovalent functionalization with $π−π*$ stacking and hydrophobic interactions rather than covalent functionalization. Therefore, graphene-based materials blended with

conjugated organic polymers are utilized for the effective exciton separation and charge transport. The large surface area for donor/acceptor interfaces and continuous pathway are responsible for the electron transfer. Hybridization of graphene with conducting polymers improves the thermal, electrical, and mechanical properties of graphene, and these composites are fabricated through melt blending,[29] in situ polymerization,[30] and solution mixing.[31] The stabilities of various graphene nanoflakes containing 42, 54, 78, 82, and 84 carbon atoms have also been studied and modeled.[32]

Graphene/polymers nanocomposite have been explored much in various forms. It was observed that better electrical and mechanical properties of nanocomposites are achieved when a small amount of graphene is added to polymers.[33] The discovery of polymer nanocomposites by the Toyota research group opened a new dimension in the field of material science. Various kinds of conducting polymer such as polypyrrole (PPy), polyacetylene (PAC), polyaniline (PANI), and polythiophene (PT) have been composited with graphene filler. An interesting feature of graphene/polymer nano-composites is the utilization of low filler loading in the polymer matrix to improve these properties. The graphene/polypyrrole and graphene/polyaniline nanocomposite are extensively used for biological application and energy storage devices while graphene/polyacetylene and graphene/polythiophene (or its derivatives)-based nanocomposites are used in optoelectronic devices.[34] The fabrication of such systems bequeathed with optoelectronic properties has become an attractive area of interest. The unique and tunable optoelectronic properties of polythiophene (PT) and graphene composites make them promising candidates for electronic devices. Polythiophene and graphene (PT/GR) composites are prepared by in situ polymerization,[35−38] plasma method,[39] and chemical polymerization.[40] Polythiophenes are π-conjugated polymers and can potentially exhibit $\pi−\pi$ interactions with carbon nanomaterials such as carbon nanotubes, graphene, and graphene oxides and are used as conductive dispersant for graphene to obtain highly conductive patterns.[41] Polythiophene and its derivatives are considered most conductive polymers as they possess the ability to conduct electricity and high charge mobility.[42]

The graphene composites with conducting polymers are not much explored theoretically and very few studies are available. Molecular dynamic simulations with Reax force field are used to study the mechanical properties of graphene/polythiophene composites.[43] The electronic, vibrational, and optical properties of polyaniline composites with edge-modified graphene quantum dots are explored theoretically by using a mix approach of molecular dynamics in the frame of DFT. Time-dependent DFT (TD-DFT) approach at the B3LYP/6-31G(d) level of theory is used to explore the optical properties and electronic dynamics[44] of these systems. The theoretical insight regarding the structure, electronic properties, and type of interaction of graphene/polythiophene composites is unknown as revealed from the literature. The current study focuses to obtain the structural details of graphene/polythiophene composites in the framework of DFT. The change in the geometric parameters of polythiophene after binding with graphene, strength of interaction between graphene and polythiophene, and the electronic properties in terms of highest occupied molecular orbital (HOMO)−lowest unoccupied molecular orbital (LUMO) gap of these composites are

evaluated, and the confirmation of structure of composites is inferred by comparison with the available experimental results.

2. COMPUTATIONAL DETAILS

All calculations are performed with Q-chem 5.2[45] and results are visualized by different graphical interface such as GaussView[46] and IQmol.[47] The various geometries of graphene nanosheets and nanoribbons with oligothiophenes are optimized at the M06-2X/6-31G(d) level of theory. Interaction energies are calculated with M06-2X/6-31G(d) (with and without dispersion correction) and ωB97M-V/def2-TZVPD. M06-2X-D3/[48−50]6-31G(d) and ωB97M-V/def2-TZVPD are counterpoise (CP)-corrected and ωB97M-V/def2-TZVPD with counterpoise correction gives a good estimate of interaction energies and is considered as the best functional for main-group thermochemical kinetics and noncovalent interactions.[51] M06-2X captures only medium-range[52] electron correlation, although it is a commonly used functional for noncovalent interactions and thermochemistry.[53] In accurate quantum-mechanical computations, long-range electron correlation must be included to reliably account for dispersion interactions. The ωB97M-V functional, which includes VV10[51] nonlocal correlation, incorporates the dispersion effects for the right physical reasons. The Karlsruhe basis set (def2-TZVPD)[54] minimizes the basis set super-position error (BSSE) that would probably appear with smaller basis set (6-31G(d)). Nonetheless, we report CP-corrected results for the ωB97M-V functional. The interaction energies of the graphene/oligothiophene nanosheet and nanoribbon composites are calculated as

$$E_{int} = E_{composite} - (E_{oligothiophene} + E_{graphene}) \qquad (1)$$

where E_{int} is the interaction energy of graphene/oligothiophene composites. $E_{composite}$, $E_{oligothiophene}$, and $E_{graphene}$ are the energies of graphene−oligothiophene composite, oligothiophene, and graphene, respectively. $E_{oligothiophene}$ and $E_{graphene}$ are calculated in supersystem basis for CP correction. The electronic properties are calculated at the B3LYP/6-31G(d) level of theory. B3LYP is an excellent functional for orbital energies and HOMO−LUMO gap calculations[55−60] The UV−visible (vis) spectra are simulated with time-dependent DFT to get the crucial excited states. Density of states (DOS) spectra are plotted using GaussSum software.[61] The noncovalent interaction index (NCI) is obtained through Multiwfn 3.6 program[62] to study the weak interaction and influence of $\pi\cdots\pi$ interactions. The reduced density gradient (RDG) color-mapped isosurfaces (0.5 au) graphs are rendered by the VMD1.9.3 program.[63] The scatter plots of reduced density gradient (RDG) versus the second largest eigenvalue of the Hessian matrix of electron density functions are obtained by Multiwfn 3.6 program.[62]

3. RESULTS AND DISCUSSION

3.1. Optimized Structures. Graphene nanosheets and nanoribbons are loaded with thiophene oligomers in various orientations to get the accurate electronic structure of graphene/polythiophene composites. The models are simulated at the M06-2X functional with 6-31G(d) basis set. The graphene sheets containing 30, 46, and 59 carbon atoms having molecular formula $C_{30}H_{14}$, $C_{46}H_{18}$, and $C_{59}H_{20}$, respectively, are selected to load with thiophene oligomers. The graphene nanoribbons having 38, 46, and 54 carbon atoms with

molecular formula $C_{38}H_{22}$, $C_{46}H_{26}$, and $C_{54}H_{30}$, respectively, are also used to stack thiophene oligomers. Experimentally reported[64,65] composites contain low percentage of graphene, so a model should be such which corresponds to actual composite. Therefore, sandwich structures are considered where one or two oligothiophene chains are placed on either side of the graphene nanosheet or nanoribbon. Three different possible orientations (vertical, tilted, and π-stacking) are considered as input files for the interaction of oligothiophene with graphene model; however, some of these structures (such as tilted orientation) converged to more stable π-stacking during optimization. The oligothiophene chain exists in anticonformation where the dihedral angle between sulfur atoms of two adjacent thiophene rings is close to 180°. For such conformation, the oligothiophene with odd number of thiophene rings presents a symmetrical structure and the number of calculations are reduced due to the symmetry of the system. Therefore, oligothiophene with odd number of thiophenes (1, 3, 5, 7, 9) are selected. Frequency calculations of some selected configurations of ribbon and sheet models are carried out to confirm that these structures are true minima on the potential energy surface. Frequency calculations on all structures are not possible mainly due to the computational cost for analytical Hessian calculations for such large systems. Therefore, frequency calculations are performed only on small composite structures. The finite-difference (FD) approach[66] is also used for some selected structures to calculate the harmonic frequencies. The FD approach to DFT harmonic frequency extends harmonic analysis to cases where analytic Hessian calculations are complicated and difficult or where the Hessian cannot be calculated easily.

3.2. Interaction Energies. The stability of graphene/polythiophene composites can be accounted from the interaction energy values. The strength of interaction between graphene sheet and ribbon composites with thiophene oligomers (n = 1, 3, 5, 7, 9, 11, 13) are studied using th DFT method at the M06-2X/6-31G(d), M06-2X-D3/6-31G(d), M06-2X-D3/6-31G(d) (CP), and ωB97M-V/def2-TZVPD (CP) levels of theory, and interaction energies are listed in Table 1 while geometric parameters are in Table S1. Counterpoise-corrected energies at ωB97M-V/def2-TZVPD (CP) are used to explain the interaction between graphene and oligothiophenes. Interaction energies of various configurations are calculated by using eq 1.

3.2.1. Interaction Energies Based on Graphene Nanosheet Composites. 3.2.1.1. $C_{30}H_{14}\cdots nPT$ Composites. The $C_{30}H_{14}$ graphene nanosheet is first stacked with nPT (n = 1, 3, 5) oligomers on one side, and their interaction energies are calculated and listed in Table 1. The counterpoise-corrected interaction energy of $C_{30}H_{14}\cdots 1PT$ at ωB97M-V/def2-TZVPD in π-stacking orientation is −8.64 kcal mol⁻¹, and the interlayer distance between graphene sheet and thiophene is 3.66 Å. The interaction energy increases to −19.98 kcal mol⁻¹ for $C_{30}H_{14}\cdots 3PT$. The interplanar distance between graphene nanosheet and oligothiophene is 3.55 Å. This increase in energy is due to increase in π···π interaction among oligothiophene and graphene sheet. The 1PT is also loaded on graphene sheet in vertical (T-shaped) orientation, and its optimized structure comes out with two types of CH−π and S−π noncovalent π interactions. The CH−π is a kind of hydrogen bond, and interaction between CH and π system is attractive.[67] The S−π[68] interaction is between thiophene sulfur and the π system of graphene sheet. The interaction energy for vertical

Table 1. Interaction Energies of Oligothiophene and Graphene Nanosheet ($C_{30}H_{14}\cdots nPT$), ($C_{46}H_{18}\cdots nPT$), ($C_{59}H_{20}\cdots nPT$), and nanoribbon ($C_{38}H_{22}\cdots nPT$), ($C_{46}H_{26}\cdots nPT$), ($C_{54}H_{30}\cdots nPT$) Models Optimized at the M06-2X/6-31G(d) versus ωB97M-V(CP)/def2-TZVPD Level

system	ωB97M-V(CP)	M06-2X	M06-2X-D3(CP)	M06-2X-D3
$C_{30}H_{14}\cdots 1PT$ (stacked)	−8.64	−5.84	−6.03	−8.63
$C_{30}H_{14}\cdots 1PT$ (T-shaped)	−5.58	−2.53	−3.99	−5.07
$C_{30}H_{14}\cdots 3PT$	−19.98	−15.84	−15.13	−20.65
$C_{30}H_{14}\cdots 5PT$	−25.56	−20.19	−19.82	−26.09
$1PT\cdots C_{30}H_{14}\cdots 1PT$	−17.64	−13.76	−12.60	−17.96
$3PT\cdots C_{30}H_{14}\cdots 3PT$	−37.83	−30.91	−29.07	−39.15
$5PT\cdots C_{30}H_{14}\cdots 5PT$	−47.73	−38.85	−37.66	−49.89
$C_{46}H_{18}\cdots 1PT$ (stacked)	−9.53	−7.79	−6.95	−9.64
$C_{46}H_{18}\cdots 1PT$ (T-shaped)	−6.37	−4.00	−4.85	−5.88
$C_{46}H_{18}\cdots 3PT$	−26.91	−22.32	−20.43	−26.74
$C_{46}H_{18}\cdots 5PT$	−35.82	−30.59	−25.32	−30.72
$1PT\cdots C_{46}H_{18}\cdots 1PT$	−19.20	−15.79	−13.98	−19.24
$3PT\cdots C_{46}H_{18}\cdots 3PT$	−53.07	−44.04	−39.41	−52.48
$5PT\cdots C_{46}H_{18}\cdots 5PT$	−71.92	−61.16	−55.22	−72.47
$C_{59}H_{20}\cdots 1PT$ (stacked)	−10.00	−9.22	−7.33	−10.02
$C_{59}H_{20}\cdots 1PT$ (T-shaped)	−7.20	−4.52	−5.85	−6.88
$C_{59}H_{20}\cdots 3PT$	−30.34	−24.15	−22.52	−28.98
$C_{59}H_{20}\cdots 5PT$	−41.79	−33.20	−30.85	−40.26
$1PT\cdots C_{59}H_{20}\cdots 1PT$	−20.11	−16.40	−14.94	−20.27
$3PT\cdots C_{59}H_{20}\cdots 3PT$	−57.40	−46.24	−42.29	−55.43
$5PT\cdots C_{59}H_{20}\cdots 5PT$	−85.07	−69.61	−63.67	−83.48
$C_{38}H_{22}\cdots 1PT$	−6.57	−6.10	−4.82	−6.94
$C_{38}H_{22}\cdots 3PT$	−19.56	−18.40	−15.73	−20.39
$C_{38}H_{22}\cdots 5PT$	−30.28	−28.40	−24.56	−32.74
$1PT\cdots C_{38}H_{22}\cdots 1PT$	−13.74	−13.00	−10.79	−15.54
$3PT\cdots C_{38}H_{22}\cdots 3PT$	−38.76	−36.20	−30.96	−42.57
$5PT\cdots C_{38}H_{22}\cdots 5PT$	−61.56	−57.50	−50.15	−68.02
$C_{46}H_{26}\cdots 3PT$	−19.80	−18.20	−14.57	−20.48
$C_{46}H_{26}\cdots 5PT$	−32.08	−30.70	−25.17	−33.93
$C_{46}H_{26}\cdots 7PT$	−41.30	−36.90	−31.62	−43.21
$3PT\cdots C_{46}H_{26}\cdots 3PT$	−39.65	−54.70	−32.78	−44.29
$5PT\cdots C_{46}H_{26}\cdots 5PT$	−64.35	−76.80	−52.76	−69.94
$7PT\cdots C_{46}H_{26}\cdots 7PT$	−82.70	−94.48	−67.47	−90.66
$C_{54}H_{30}\cdots 3PT$	−19.20	−16.70	−13.37	−18.97
$C_{54}H_{30}\cdots 5PT$	−31.62	−28.40	−23.35	−32.20
$C_{54}H_{30}\cdots 7PT$	−43.29	−39.00	−33.12	−45.01
$C_{54}H_{30}\cdots 9PT$	−51.49	−46.60	−40.44	−55.02
$C_{54}H_{30}\cdots 11PT$	−55.34	−49.81	−43.79	−59.04
$C_{54}H_{30}\cdots 13PT$	−55.65	−49.82	−43.95	−59.58
$3PT\cdots C_{54}H_{30}\cdots 3PT$	−70.96	−61.01	−54.52	−66.26
$5PT\cdots C_{54}H_{30}\cdots 5PT$	−96.57	−78.11	−75.30	−92.62
$7PT\cdots C_{54}H_{30}\cdots 7PT$	−120.13	−100.68	−94.55	−118.27
$9PT\cdots C_{54}H_{30}\cdots 9PT$	−135.40	−101.94	−107.14	−134.67

orientation is −5.58 kcal mol⁻¹, and the S−π distance and CH−π distance are 3.76 and 2.93 Å, respectively. The $C_{30}H_{14}\cdots 3PT$ composite is also optimized in vertical orientation, but 3PT does not remain vertical and becomes parallel (π stacking) to graphene sheet after optimization. The interaction energy values reveal that π···π interactions are stronger in π-stacking configuration than CH−π and S−π
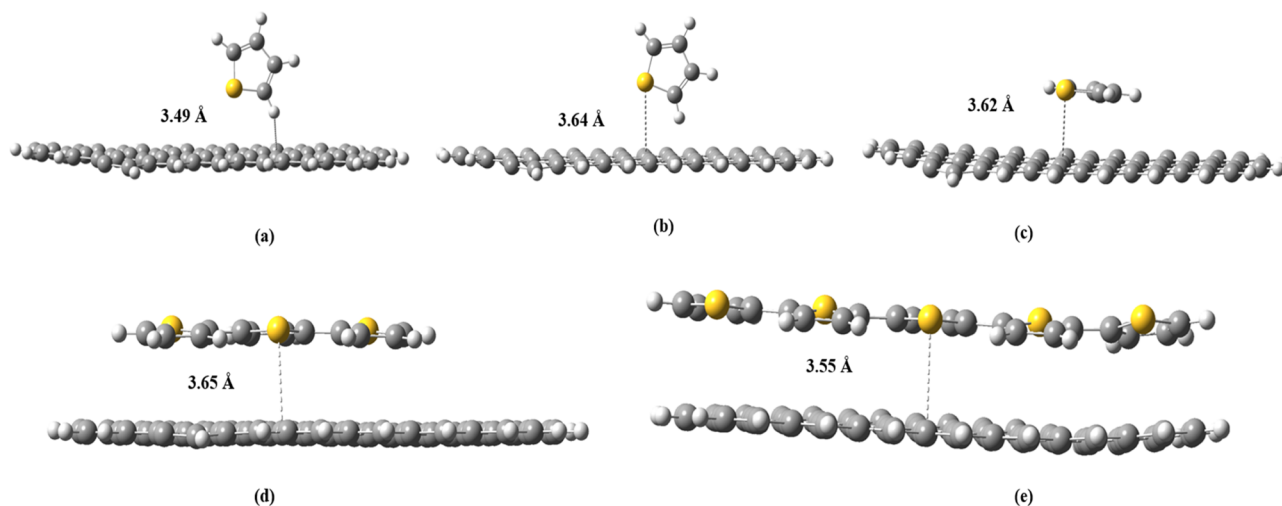
Figure 1. Optimized geometries of (a) vertical CH···π, (b) vertical S···π, (c) stacked $C_{59}H_{20}$···1PT, (d) $C_{59}H_{20}$···3PT, and (e) $C_{59}H_{20}$···5PT composites.

bonds in vertical (T-shaped) orientation. The interaction energy for the $C_{30}H_{14}$···5PT composite is −25.56 kcal mol^{-1}, and the average interplanar distance is 3.44 Å. The π-stacking orientation is more stable than tilted and vertical because π···π interactions are stronger. These interactions are noncovalent in nature and operate in molecules having π system. The π-stacking $C_{30}H_{14}$···5PT composite is more stable than the $C_{30}H_{14}$···3PT and $C_{30}H_{14}$···1PT composites as oligothiophene becomes more parallel to graphene sheet and increases the extent of conjugation and delocalization of π electrons in $C_{30}H_{14}$···5PT composite. The optimized structures with interlayer distance are shown in Figure S1 of the Supporting Information.

3.2.1.2. nPT···$C_{30}H_{14}$···nPT Composites. This model of graphene sheet is also sandwiched between two oligothiophene chains, and optimized configurations are shown in Figure S2 (Supporting Information). These configurations are studied in π-stacking orientation. The interaction energy (CP) for the 1PT···$C_{30}H_{14}$···1PT composite is −17.46 kcal mol^{-1}. The interplanar distance of 1PT···$C_{30}H_{14}$···1PT for side A is 3.32 Å and that for side B is 3.36 Å. These distances are much smaller than 3.66 Å for 1PT···$C_{30}H_{14}$.

The interaction energy for 3PT···$C_{30}H_{14}$···3PT composite is −37.83 kcal mol^{-1} and the interplanar distance between side A is 3.53 Å and side B is 3.83 Å. The interaction energy increases as the size of oligothiophene increases. The interaction energy of the 5PT···$C_{30}H_{14}$···5PT composite is −47.73 kcal mol^{-1}. The interplanar distance for side A is 3.63 Å and that for side B is 3.28 Å. The stability of the composite increases with increase in chain length. These chains interact with graphene sheet through π···π interactions.

3.2.1.3. $C_{46}H_{18}$···nPT Composites. In this model, graphene nanosheet ($C_{46}H_{18}$) is loaded with thiophene oligomers having one, three, and five units. The composites are optimized in π-stacking orientation, and their interaction energies are calculated. The vertical orientation is studied for only the $C_{46}H_{18}$···1PT composite. The computed interaction energies are listed in Table 1, and optimized structures are depicted in Figure S3. The interplanar distance between graphene sheet and 1PT for π stacking is 3.66 Å, and for vertical orientation with two types of CH−π and S−π noncovalent π interactions, they are 3.94 and 3.50 Å, respectively. The interaction energy

of the $C_{46}H_{18}$···1PT composite with π stacking orientation is −9.53 kcal mol^{-1}, and for vertical orientation, it is −6.37 kcal mol^{-1}. The interaction energy value shows that π stacking orientation is more stable than vertical orientation. Moreover, the π stacking with this model is more stable than the π stacking with the previous model, which is probably attributed to a large surface available with the $C_{46}H_{18}$ model for better interaction with oligothiophene. The interaction energy of the $C_{46}H_{18}$···1PT composite shows that it is more stable than the above-mentioned $C_{30}H_{14}$···1PT composite. The greater stability of the $C_{46}H_{18}$···1PT composite is due to a relatively large graphene sheet. This large sheet results in more effective delocalization of π electrons and favors strong π···π interactions between graphene sheet and 1PT. The interplanare distances in $C_{46}H_{18}$···3PT and $C_{46}H_{18}$···5PT composites with π stacking orientation are 3.64 and 3.63 Å, respectively. The interaction energy values for $C_{46}H_{18}$···3PT and $C_{46}H_{18}$···5PT are −26.91 and −35.82 kcal mol^{-1}, respectively. Among these, the $C_{46}H_{18}$···5PT composite is more stable due to greater π···π interaction between oligothiophene and graphene sheet because the stability of composite is affected by the length of oligothiophene.

3.2.1.4. nPT···$C_{46}H_{18}$···nPT Composites. Now this model of graphene sheet is sandwiched between two oligothiophene chains, and optimized structures are shown in Figure S4. These configurations are studied in π-stacking orientation. The interaction energy for the 1PT···$C_{46}H_{18}$···1PT composite is −19.20 kcal mol^{-1}. The interplanar distance of 1PT···$C_{46}H_{18}$···1PT for side A is 3.64 Å and that for side B is 3.45 Å. The interaction energy for the 3PT···$C_{46}H_{18}$···3PT composite is −53.07 kcal mol^{-1}, and the interplanar distances on side A and B are 3.68 and 3.79 Å, respectively. The interaction energy increases as the size of oligothiophene increases. The interaction energy of the 5PT···$C_{46}H_{18}$···5PT composite is −71.92 kcal mol^{-1}. The interplanar distance for side A is 3.67 Å and that for side B is 3.69 Å. The stability of the composite increases with increase in chain length. This is because that the long chain of oligothiophene induces more conjugation and delocalization of π electrons, which results in more effective π···π interactions with the graphene sheet. The π···π interactions on both sides of graphene sheet result in stronger

adsorption and therefore the stability of graphene/polythiophene composites.

3.2.1.5. $C_{59}H_{20}\cdots nPT$ Composites. The interaction energies of the $C_{30}H_{14}\cdots nPT$ and $C_{46}H_{18}\cdots nPT$ model reveal that the stability of composites increases as the size of graphene nanosheet increases. The same trend in stability is also observed for the oligothiophene chain. The stability is increased with the increase in the length of the oligothiophene chain. All other composites are optimized in π stacking orientation, and their interaction energies are calculated and listed in Table 1. The vertical orientation is studied for only the $C_{59}H_{20}\cdots 1PT$ composite. The interplanar distance between the graphene sheet and 1PT for π stacking is 3.62 Å, and for vertical orientation with CH−π, it is 3.49 Å, and with S−π, it is 3.64 Å. The interaction energy of the $C_{59}H_{20}\cdots 1PT$ composite with π-stacking orientation is −10.0 kcal mol^{-1}, and with vertical orientation, it is −7.20 kcal mol^{-1}, and the optimized structures are depicted in Figure 1. The interaction energy value shows that again π-stacking orientation is more stable than vertical orientation. The interaction energy of the $C_{59}H_{20}\cdots 1PT$ composite shows that it is more stable than the above models of graphene/polythiophene composites. The larger graphene sheet results in more effective delocalization of π electrons and favors strong $\pi\cdots\pi$ interactions between graphene sheet and 1PT. The interplanar distances in $C_{59}H_{20}\cdots 3PT$ and $C_{59}H_{20}\cdots 5PT$ composites with π stacking orientation are 3.65 and 3.55 Å, respectively. The interaction energy value for the $C_{59}H_{20}\cdots 3PT$ composite is −30.34 kcal mol^{-1} and that for the $C_{59}H_{20}\cdots 5PT$ composite is −41.79 kcal mol^{-1}.

3.2.1.6. $nPT\cdots C_{59}H_{20}\cdots nPT$ Composites. The $C_{59}H_{20}$ graphene sheet model is sandwiched between two oligothiophene chains in π-stacking orientation, and optimized configurations are shown in Figure S5. The interaction energy for the $1PT\cdots C_{59}H_{20}\cdots 1PT$ composite is −20.11 kcal mol^{-1}. The interplanar distances of $1PT\cdots C_{59}H_{20}\cdots 1PT$ for sides A and B are 3.75 and 3.46 Å, respectively. The interaction energy for the $3PT\cdots C_{59}H_{20}\cdots 3PT$ composite is −57.40 kcal mol^{-1}, and the interplanar distances for sides A and B are 3.62 and 3.34 Å, respectively. The interaction energy increases as the size of oligothiophene increases. For $5PT\cdots C_{30}H_{14}\cdots 5PT$, the interaction energy is −85.07 kcal mol^{-1} and the interplanar distances for sides A and B are 3.60 and 3.29 Å, respectively. The stability of the composite increases with increase in chain length of oligothiophene and the size of graphene sheet. The vertical orientation of thiophene on all models of graphene sheet is less stable than π-stacking orientation. This is because in vertical orientation CH−π and S−π interactions arise, which causes less binding of oligothiophene on graphene sheet. In π-stacking orientation, the conjugation and delocalization of π electrons result in more effective $\pi\cdots\pi$ interactions with the graphene sheet. The interaction energies of different sheet models reveal that it increases with increase in the size of graphene sheet and oligothiophenes. The $C_{59}H_{20}\cdots nPT$ composites show maximum values of interaction energies among $C_{46}H_{18}\cdots nPT$ $C_{30}H_{18}\cdots nPT$ composites due to a larger graphene sheet. The larger graphene sheet increases the conjugation of π electrons, which also increases $\pi\cdots\pi$ interactions among oligothiophenes and graphene sheet and gives more stable composites.

3.2.2. Interaction Energies Based on Graphene Nanoribbon Composites. The synthesis of graphene/polythiophene composites and their performance as supercapacitors[69] and energy storage devices[40] have been studied experimentally.

The composites with increasing concentration of graphene are also reported.[65] The concentration of graphene changes the optical properties of composites. The concentration of graphene is increased by using graphene nanoribbons containing 38, 46, and 54 carbon atoms. The graphene nanosheet-based composites are more stable in π-stacking orientation than tilted and vertical orientations. Therefore, only π-stacking orientation of oligothiophene on graphene nanoribbons is studied.

3.2.2.1. $C_{38}H_{22}\cdots nPT$ Composites. Graphene nanoribbons are loaded with one, three, and five units of oligothiophene in π-stacking orientation to explore the correct electronic structure and optical properties of graphene/polythiophene composites. The graphene ribbons are also sandwiched by increasing the concentration of polythiophene. The interaction energy for the $C_{38}H_{22}\cdots 1PT$ composite is −6.75 kcal mol^{-1} (Table 1) with an interplanar distance of 3.67 Å. The interaction energy increases to −19.56 kcal mol^{-1}, and the distance decreases to 3.65 Å when graphene nanoribbon is loaded with 3PT. The oligothiophene remains flat on graphene ribbon. The interaction energy increases to −30.28 kcal mol^{-1}, and the distance decreases to 3.56 Å in $C_{38}H_{22}\cdots 5PT$. The graphene ribbon gets bent at the center when loaded with 5PT, as shown in Figure S6c. The oligothiophene does not remain planar as their length increases, and this change in planarity also affects the geometry of graphene ribbon and it bends at the center due to effective $\pi\cdots\pi$ interactions among them. The interaction energy increases with increase in chain length, which, in turn, demonstrates an increase in the stability of composites.

3.2.2.2. $nPT\cdots C_{38}H_{22}\cdots nPT$ Composites. The interaction energy of the $1PT\cdots C_{38}H_{22}\cdots 1PT$ composite is −13.74 kcal mol^{-1}, and the interplanar distances on side A and side B are 3.17 and 4.3 Å, respectively. The interaction energy increases to −38.76 kcal mol^{-1} in $3PT\cdots C_{38}H_{22}\cdots 3PT$ with an interplanar distance of 3.7 Å on side A and 4.2 Å on side B, and −61.56 kcal mol^{-1} for $5PT\cdots C_{38}H_{22}\cdots 5PT$ composites. The 3PT remains flat on both sides of ribbons, but 5PT is slightly bent on edges. The interaction energy of the $5PT\cdots C_{38}H_{22}\cdots 5PT$ composite is −61.56 kcal mol^{-1}, and the interplanar distances on side A and side B are 3.8 and 3.5 Å, respectively. The increase in energy reflects an increase in the stability of composites, and this is attributed to increase in conjugation between graphene ribbon and oligothiophene. The optimized structures of the composites are shown in Figure S7. This effective delocalization increases the $\pi\cdots\pi$ interaction among composites.

3.2.2.3. $C_{46}H_{26}\cdots nPT$ Composites. This model of graphene ribbon is loaded with one, three, and seven units of PT on one side and on both sides in π-stacking orientation, and the optimized structures are depicted in Figures S8 and S9. Their interaction energies are calculated and listed in Table 1. The interaction energy of the $C_{46}H_{26}\cdots 3PT$ composite is −19.80 kcal mol^{-1} with an interplanar distance of 3.9 Å. The energy increases to −32.08 kcal mol^{-1} for $C_{46}H_{26}\cdots 5PT$ and −41.30 kcal mol^{-1} for $C_{46}H_{26}\cdots 7PT$ composites. The increase in interaction energy results as the conjugation increases with increase in oligothiophene chain. The interplanar distances decrease to 3.70 and 3.60 Å for $C_{46}H_{26}\cdots 5PT$ and $C_{46}H_{26}\cdots 7PT$, respectively. The decrease in interplanar distances also supports the increase in interaction energies among them. The change in the geometry of graphene ribbon is also observed as oligothiophene does not remain planar in higher composites.
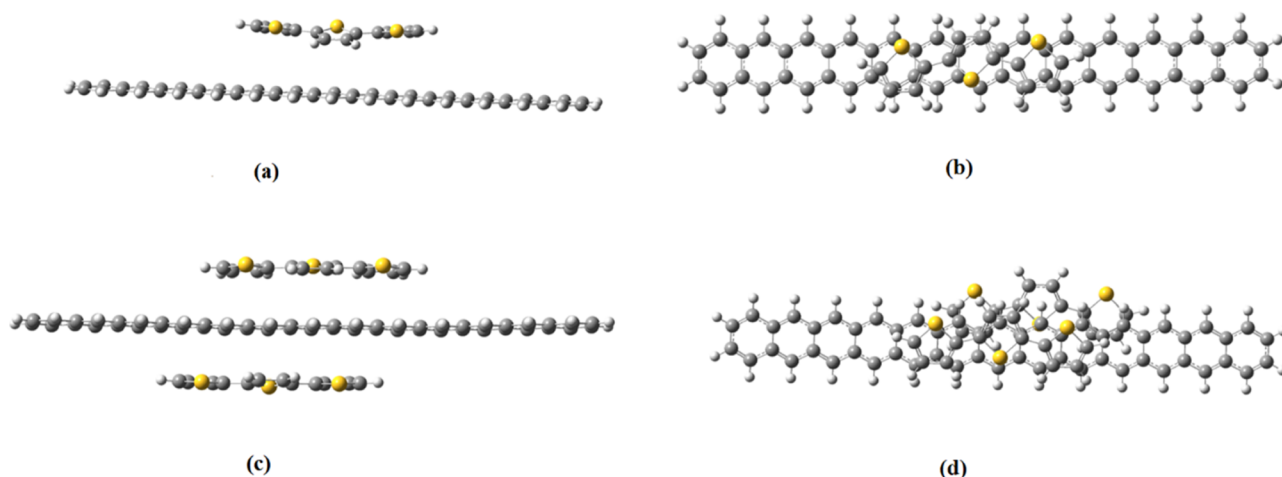
Figure 2. (a, c) Side and (b, d) top views of stacked $C_{54}H_{30}\cdots3PT$ and $3PT\cdots C_{54}H_{30}\cdots3PT$ composites.
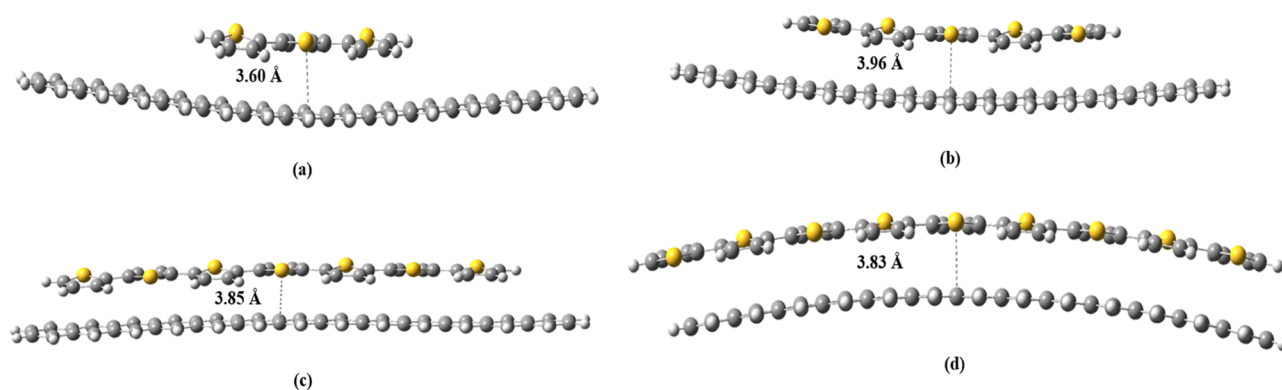
Figure 3. Optimized geometries of (a) stacked $C_{54}H_{30}\cdots3PT$, (b) $C_{54}H_{30}\cdots5PT$, (c) $C_{54}H_{30}\cdots7PT$, and (d) $C_{54}H_{30}\cdots9PT$ composites.

3.2.2.4. $nPT\cdots C_{46}H_{26}\cdots nPT$ Composites. The interaction energy of complexes increases with increase in chain length. The interaction energy for the $3PT\cdots C_{46}H_{26}\cdots3PT$ sandwich composite is -39.65 kcal mol^{-1}. The distances between 3PT and graphene ribbon on sides A and B are 3.83 and 4.42 Å, respectively. The interaction energy increases to -64.35 kcal mol^{-1} by increasing the chain length of oligothiophene on both sides of graphene ribbon in $5PT\cdots C_{46}H_{26}\cdots5PT$ composites. The interplanar distance decreases to 3.82 Å on side A and to 4.41 Å on side B. The interaction energy for $7PT\cdots C_{46}H_{26}\cdots7PT$ composites increases to -82.70 kcal mol^{-1}. The distance decreases as 7PT does not remain flat on graphene ribbon surface but bent away from planarity on edges and bent toward graphene ribbon at the center of oligothiophene. This bending toward the ribbon from the center decreases the distance from side A to 3.63 and 3.52 Å from side B. The $\pi\cdots\pi$ interaction increases between oligothiophene and graphene ribbon with increase in chain length.

3.2.2.5. $C_{54}H_{30}\cdots nPT$ Composites. This model of graphene ribbon is loaded with 3, 5, 7, 9, 11, and 13 units of PT on one side in π stacking orientation, and their interaction energies are calculated (Table 1). The interaction energy of the $C_{54}H_{30}\cdots$ 3PT composite is -19.20 kcal mol^{-1}, and the interplanar distance is 3.60 Å. The optimized configurations are shown in Figure 3 with side and top views of $C_{54}H_{30}\cdots3PT$ composite in Figure 2. The energy increases to -31.62 kcal mol^{-1} for $C_{54}H_{30}\cdots5PT$ and to -43.29 kcal mol^{-1} for $C_{54}H_{30}\cdots7PT$ composites. The distances between oligothiophene and

graphene ribbon for 5PT and 7PT composites are 3.96 and 3.85 Å, respectively. The interaction energy for $C_{54}H_{30}\cdots9PT$ is -51.49 kcal mol^{-1}, whereas the interaction distance is 3.83 Å. The $C_{54}H_{30}\cdots11PT$ and $C_{54}H_{30}\cdots13PT$ composites have -55.34 and -55.65 kcal mol^{-1} energies, respectively. Both complexes have a similar interplanar distance (3.84 Å). The energy increases with increase in chain length of oligothiophene; the increase is appreciable up to 9 oligomers and after that, the change in energy is almost same. The $C_{54}H_{30}\cdots nPT$ ribbon composites show maximum values of interaction energies among $C_{46}H_{26}\cdots nPT$ $C_{38}H_{22}\cdots nPT$ composites due to increase in the length of graphene ribbon.

3.2.2.6. $nPT\cdots C_{54}H_{30}\cdots nPT$ Composites. This model is sandwiched by loading three, five, seven, and nine oligothiophenes on both sides of graphene ribbon, and their interaction energies are calculated (Table 1). The three and five oligothiophenes slide little above and below the graphene ribbon after optimization, as shown in Figure 4a,b. The interaction energy of the $3PT\cdots C_{54}H_{30}\cdots3PT$ composite is -70.96 kcal mol^{-1}, and the distance on side A is 3.58 Å and on side B is 4.74 Å. Some of the sandwich complexes show superadditivity of interaction energies. For $3PT\cdots C_{54}H_{30}$, the interaction energy is -19.20 kcal mol^{-1}, and it is expected that the sandwich complex $3PT\cdots C_{54}H_{30}\cdots3PT$ will show twice the interaction energy ($2 \times -19.20 = -38.40$ kcal mol^{-1}). However, the complex shows about -32.56 kcal mol^{-1} higher interaction energy, which illustrates the superadditivity of the interaction energies. The superadditivity may be attributed to
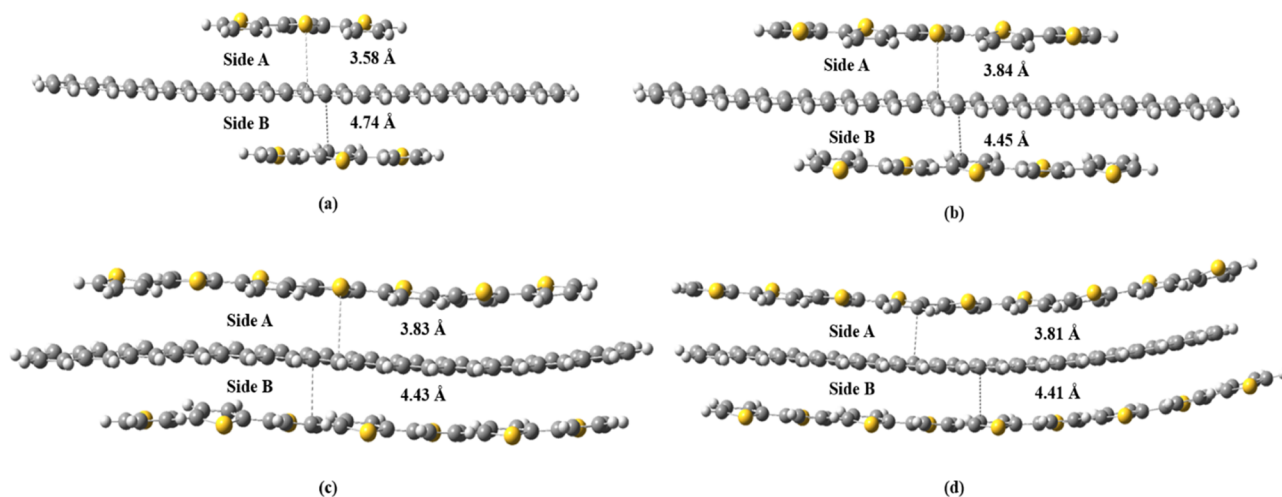
Figure 4. Optimized geometries of (a) stacked 3PT···C$_{54}$H$_{30}$···3PT, (b) 5PT···C$_{54}$H$_{30}$···5PT and (c) 7PT···C$_{54}$H$_{30}$···7PT, and (d) 9PT···C$_{54}$H$_{30}$···9PT composites.

polarization of graphene nanosheet by first oligothiophene, which facilitates the incoming of the second oligothiophene.

The interaction energy of the 5PT···C$_{54}$H$_{30}$···5PT composite is −96.57 kcal mol^{-1}. The interaction of two oligothiophenes with graphene ribbon in sandwich composites of nPT···C$_{46}$H$_{26}$···nPT and nPT···C$_{54}$H$_{30}$···nPT leads to superadditivity of interaction energy, in which the interaction energy of the oligothiophenes exceeds the simple sum of the interaction energies of individual components. This overproportional increase or superadditivity is attributed to the fact that the first oligothiophene causes the polarization of graphene ribbon, which opens the path for the second oligothiophene to interact with graphene ribbon. The distance between graphene ribbon and 5PT on side A is 3.84 Å and on side B is 4.45 Å. The energy increases to −120.13 and −135 kcal mol^{-1} for 7PT···C$_{54}$H$_{30}$···7PT and 9PT···C$_{54}$H$_{30}$···9PT composites, respectively. The distance between oligothiophene and graphene nanoribbon on side A is 3.83 Å and on side B is 4.43 Å for 7PT, and for 9PT, it is 3.81 Å on side A and 4.41 Å on side B. The energy increases as the length of PT chain increases on both sides, and the stability also increases. In π-stacking orientation, the conjugation and delocalization of π electrons results in more effective π···π interactions with the graphene sheet. The π···π interactions increase with the size of graphene sheet and the chain of thiophene oligomers.

The C$_{54}$H$_{30}$ graphene ribbon model is also optimized by increasing the amount of oligothiophene 2 times on both sides of graphene. The interaction energy increases to −193.02 kcal mol^{-1}. The distance on one side of graphene ribbon and 9PT is represented as A′, whereas the distance between two 9PT oligomers is represented as A″. Similarly, B′ and B″ are the similar corresponding distances on the other side of ribbon. The values of A′, A″, B′, and B″ are 3.67, 3.76, 3.47, and 3.24 Å, respectively, as shown in Figure S11. The length of graphene ribbon also increases the extent of interactions among oligothiophene and nanoribbons. The PT chains remain stacked on the surface of ribbon and increases the π···π interactions. Moreover, composites with double amount of PT are more stable than their single-chain analogue. The delocalization increases, which results in effective π···π interactions. The comparison of the interaction energy values of graphene sheet and ribbon models with oligothiophenes

shows that ribbon models are more stable as their interaction energies are higher than sheet models. The maximum interaction energy of the ribbon model is −193.02 kcal mol^{-1} higher than −85.07 kcal mol^{-1} of sheet model. The interaction energies are computed with different methods. The ωB97M-V(CP)/def2-TZVPD gives a good estimate of interaction energies within infinite basis set limit compared to M06-2x/6-31G(d) to capture the noncovalent interactions. The comparison of basis set with these two methods in terms of interaction energy is shown in Figure S12. An astounding correlation in the interaction energies is also observed in the long-range (-D3) part of the M06-2X-D3 and the basis set superposition error (BSSE) in the M06-2X functional in Figure S13. The magnitudes of dispersion correction (D3) from the M06-2X-D3 method are given in Table S1 (Supporting Information).

3.3. Orbital Analysis. *3.3.1. Pristine Polythiophene.* The energies of HOMO and LUMO (frontier orbitals) of polythiophene are changed when composited with graphene. Graphene lowers the optical band gap of polythiophene by forming mid-gap state, and the conductivity of graphene/polythiophene composites increases with decrease in band gap. HOMO−LUMO energy gaps are calculated at the B3LYP/6-31G(d) level of theory because B3LYP is a reliable functional for the simulation of electronic properties.[55] Further validation of the B3LYP method is done by comparison of the theoretically calculated optical gap with the available experimental data. The experimental optical band gap for polythiophene is 2.23 eV.[70] The optical band gap calculated for 9PT at the B3LYP/6-31G(d) level is 2.3 eV, which agrees nicely with the experimental value of 2.23 eV. We have shown previously that the properties of a nine-unit oligomer nicely present the properties of polymer, more particularly regarding the HOMO−LUMO gap. The excellent correlation gives us confidence that B3LYP is an accurate functional for optical band gap calculations.[71] The band gap decreases with increase in chain length of oligothiophene, and the results are listed in Table 2. The decrease in optical band gap reflects in an increase in the conductivity of oligothiophenes.

3.3.2. C$_{30}$H$_{14}$···nPT Composites. Energies of HOMO, LUMO, and HOMO−LUMO gap are calculated at the B3LYP/6-31G(d) level of theory. The HOMO, LUMO

Table 2. Optical Band Gap, λ_{max}, Oscillator Strength, and Excitation Energy of Oligothiophene- and Graphene Nanosheet-Based ($C_{30}H_{14}\cdots n$PT), ($C_{46}H_{18}\cdots n$PT), and ($C_{59}H_{20\ldots}n$PT) Composites

model	HOMO−LUMO gap (eV) B3LYP/6-31G(d)	λ_{max} (nm)	oscillator strength	excitation energy (eV)
$C_{30}H_{14}\cdots$1PT	2.28	420	1.04	2.95
$C_{30}H_{14}\cdots$3PT	2.27	319	0.63	3.89
$C_{30}H_{14}\cdots$5PT	2.26	375	1.56	3.27
1PT$\cdots C_{30}H_{14}\cdots$1PT	2.27	427	0.96	3.89
3PT$\cdots C_{30}H_{14}\cdots$3PT	2.27	319	0.76	2.97
5PT$\cdots C_{30}H_{14}\cdots$5PT	2.26	418	2.55	3.87
$C_{46}H_{18}\cdots$1PT	1.23	320	1.81	3.98
$C_{46}H_{18}\cdots$3PT	1.24	311	0.73	3.83
$C_{46}H_{18}\cdots$5PT	1.25	324	1.22	3.87
1PT$\cdots C_{46}H_{18}\cdots$1PT	1.23	320	1.41	1.67
3PT$\cdots C_{46}H_{18}\cdots$3PT	1.24	742	0.33	3.21
5PT$\cdots C_{46}H_{18}\cdots$5PT	1.26	386	0.32	3.18
$C_{59}H_{20}\cdots$1PT	0.46	389	0.31	2.78
$C_{59}H_{20}\cdots$3PT	0.46	445	0.30	2.36
$C_{59}H_{20}\cdots$5PT	0.46	525	0.17	3.16
1PT$\cdots C_{59}H_{20}\cdots$1PT	0.46	392	0.23	2.81
3PT$\cdots C_{59}H_{20}\cdots$3PT	0.46	441	0.23	2.14
5PT$\cdots C_{59}H_{20}\cdots$5PT	0.50	579	0.10	3.98

energies and optical band gap values of $C_{30}H_{14}\cdots n$PT nanosheet composites are listed in Table 2, and densities are shown in Figure S14. The HOMO−LUMO gap of pristine 1PT is 6.20 eV, and for vertical and π-stacking orientations of the $C_{30}H_{14}\cdots$1PT composite at the B3LYP level, it is 2.28 eV. The lowering of band gap results in an increase in the conductivity of composite. The optical bad gap decreases to 2.27 and 2.26 eV in $C_{30}H_{14}\cdots$3PT and $C_{30}H_{14}\cdots$5PT composites, respectively. The conjugation and delocalization of π electron increases with increase in chain length of oligothiophenes, which results in lowering of band gap. The optical band gap for 1PT$\cdots C_{30}H_{14}\cdots$1PT and 3PT$\cdots C_{30}H_{14}\cdots$3PT sandwich composites is 2.27 eV, whereas the optical band gap for the 5PT$\cdots C_{30}H_{14}\cdots$5PT composite is 2.26 eV. The band gap does not change considerably in sandwich composites by increasing the number of oligothiophene units as these composites contain low concentration of graphene. Generally, the optical gap increases when oligothiophene chain length is increased on graphene nanosheet.

3.3.3. $C_{46}H_{18}\cdots n$PT Composites. HOMO, LUMO energies and HOMO−LUMO gap are calculated at the B3LYP/6-31G(d) level of theory. The optical band gap for vertical and π-stacking orientations of $C_{46}H_{18}\cdots$1PT is 1.23 eV. The band gap remains same for the $C_{46}H_{18}\cdots$1PT composite irrespective of different orientations. The band gap of 1PT is reduced to a much lower value when loaded with $C_{46}H_{18}$ compared to pristine 1PT, and this decrease is possibly due to large concentration of graphene. The HOMO−LUMO gap for $C_{46}H_{18}\cdots$3PT is 1.24 eV and remains same for the $C_{46}H_{18}\cdots$5PT composite. The calculated band gaps for sandwich composites 1PT$\cdots C_{46}H_{18}\cdots$1PT and 3PT$\cdots C_{46}H_{18}\cdots$3PT are similar to their one-sided composites. The optical gap for 5PT$\cdots C_{46}H_{18}\cdots$5PT composites is 1.26 eV, and this slight increase is due to increase in the length of oligothiophene. The band gap does not change much when the length of oligomer is increased, and it is attributed to the large proportion of graphene in the composite. The comparison of the band gaps

of $C_{30}H_{14}\cdots n$PT (2.26 eV) and $C_{46}H_{18}\cdots n$PT (1.24 eV) composites shows that it decreases rapidly as the concentration of graphene increases in composites (Table 2).

3.3.4. $C_{59}H_{20}\cdots n$PT Composites. The optical band gap values and the HOMO and LUMO energies at the B3LYP/6-31G(d) level of theory are listed in Table 2, and densities are shown in Figure S16. The calculated band gap for vertical and π-stacking orientations of $C_{59}H_{20}\cdots$1PT is 0.46 eV and remains same for $C_{59}H_{20}\cdots$3PT and $C_{59}H_{20}\cdots$5PT composite. The band gap decreases when the concentration of graphene is increased in these composites compared to pristine 1PT, and this decrease is possibly due to large concentration of graphene. The optical band gap of 1PT$\cdots C_{59}H_{20}\cdots$1PT and 3PT$\cdots C_{59}H_{20}\cdots$3PT sandwich composites remains same as that of their one-sided composites and increases to 0.50 eV for the 5PT$\cdots C_{59}H_{20}\cdots$5PT composite. This increase in the optical band gap of 5PT$\cdots C_{59}H_{20}\cdots$5PT is due to increase in length of the oligothiophene chain. The $C_{59}H_{20}\cdots n$PT composites show maximum change in band gap compared to $C_{30}H_{14}\cdots n$PT and $C_{46}H_{18}\cdots n$PT composites. This variation in band gap is observed due to increase in the concentration of graphene. The band gap decreases due to increase in conjugation and delocalization of π electrons as the size of graphene sheet is increased. Generally, the band gap decreases as the length of pristine oligothiophene increases. The band gap of composites increases and sometimes remain same as the length of oligothiophene increases as the change in optical band gap is mainly influenced by the concentration of graphene in composites.

3.3.5. $C_{38}H_{22}\cdots n$PT Composites. Graphene nanoribbons are composed of polythiophene, and their optical band gap and HOMO, LUMO energies are calculated at the B3LYP/6-31G(d) level of theory. The results are listed in Table 3, and densities are shown in Figure S17. The optical band gap of pristine 1PT is 6.20 eV, and it is reduced to 1.15 eV when composited with $C_{38}H_{22}$ graphene nanoribbon. The optical band gaps of $C_{38}H_{22}\cdots$3PT and $C_{38}H_{22}\cdots$5PT are 1.15 and 1.16 eV, respectively. The nanoribbons are sandwiched between two oligothiophene chains, and the band gap remains the same for 1PT$\cdots C_{38}H_{22}\cdots$1PT at 1.16 eV and increases to 1.18 eV for 3PT$\cdots C_{38}H_{22}\cdots$3PT and 5PT$\cdots C_{38}H_{22}\cdots$5PT composites. The band gap in composites decreases by increasing the concentration of graphene, and in sandwich composites, the concentration of graphene decreases and hence band gap increases.

3.3.6. $C_{46}H_{26}\cdots n$PT Composites. The optical band gap of the $C_{46}H_{26}\cdots$3PT composite is 0.56 eV (Table 3 and Figure S18). The band gap reduces compared to the $C_{38}H_{22}\cdots n$PT composite due to increase in concentration of graphene. The band gap also decreases when the length of oligothiophene increases in one-sided composites. The optical band gap is 0.54 eV for $C_{46}H_{26}\cdots$5PT and 0.53 eV for $C_{46}H_{26}\cdots$7PT composites. The $C_{46}H_{26}$ ribbon is also sandwiched between oligothiophene chains. The band gap increases in these composites as the concentration of graphene decreases. The optical band gap for 3PT$\cdots C_{46}H_{26}\cdots$3PT composite is 0.88 eV compared to 0.56 eV for $C_{46}H_{26}\cdots$3PT composite. The computed values of optical band gap for 5PT$\cdots C_{46}H_{26}\cdots$5PT and 7PT$\cdots C_{46}H_{26}\cdots$7PT are 0.94 and 0.93 eV, respectively. The increase in optical band gap for sandwich complexes (compared to one-sided) composite is attributed to decrease in the concentration of graphene.

Table 3. Optical Band Gap, λ_{max}, Oscillator Strength, and Excitation Energy of Oligothiophene- and Graphene Nanoribbon-Based ($C_{38}H_{22}...nPT$), ($C_{46}H_{26}...nPT$), and ($C_{54}H_{30}...nPT$) Composites

model	HOMO−LUMO gap (eV) B3LYP/6-31G(d)	λ_{max} (nm)	oscillator strength	excitation energy (eV)
$C_{38}H_{22}\cdots 1PT$	1.15	314	7.74	3.95
$C_{38}H_{22}\cdots 3PT$	1.15	304	7.89	4.08
$C_{38}H_{22}\cdots 5PT$	1.16	307	4.48	4.04
$1PT\cdots C_{38}H_{22}\cdots 1PT$	1.16	315	6.58	3.94
$3PT\cdots C_{38}H_{22}\cdots 3PT$	1.18	317	0.58	3.90
$5PT\cdots C_{38}H_{22}\cdots 5PT$	1.18	347	0.28	3.57
$C_{46}H_{26}\cdots 3PT$	0.56	500	8.32	2.47
$C_{46}H_{26}\cdots 5PT$	0.54	530	5.76	2.34
$C_{46}H_{26}\cdots 7PT$	0.53	392	5.46	3.16
$3PT\cdots C_{46}H_{26}\cdots 3PT$	0.88	360	1.89	3.44
$5PT\cdots C_{46}H_{26}\cdots 5PT$	0.94	431	0.23	2.87
$7PT\cdots C_{46}H_{26}\cdots 7PT$	0.93	419	0.89	2.96
$C_{54}H_{30}\cdots 3PT$	0.63	560	8.18	2.22
$C_{54}H_{30}\cdots 5PT$	0.60	582	7.08	2.13
$C_{54}H_{30}\cdots 7PT$	0.58	587	6.11	2.11
$C_{54}H_{30}\cdots 9PT$	0.58	590	6.03	2.10
$C_{54}H_{30}\cdots 11PT$	0.58	592	6.01	2.09
$C_{54}H_{30}\cdots 13PT$	0.58	594	6.17	2.08
$3PT\cdots C_{54}H_{30}\cdots 3PT$	0.70	368	3.85	3.37
$5PT\cdots C_{54}H_{30}\cdots 5PT$	0.73	465	0.22	2.72
$7PT\cdots C_{54}H_{30}\cdots 7PT$	0.75	426	0.75	2.91
$9PT\cdots C_{54}H_{30}\cdots 9PT$	0.75	446	0.36	2.78

3.3.7. $C_{54}H_{30}\cdots nPT$ Composites. The optical band gap of $C_{54}H_{30}\cdots nPT$ nanoribbon composites are given in Table 3, while densities are shown in Figure 5. The calculated band gaps of $C_{54}H_{30}\cdots 3PT$, $C_{54}H_{30}\cdots 5PT$, and $C_{54}H_{30}\cdots 7PT$ are

0.63, 0.60, and 0.58 eV, respectively. The band gap decreases with increase in the length of oligothiophene chain up to 7PT and then remains same for $C_{54}H_{30}\cdots 9PT$, $C_{54}H_{30}\cdots 11PT$, and $C_{54}H_{30}\cdots 13PT$. The concentration of graphene decreases in all these composites, and conductivity does not change with increase in length of the oligothiophene chain. The optical band gaps of sandwich composites of $3PT\cdots C_{54}H_{30}\cdots 3PT$ and $5PT\cdots C_{54}H_{30}\cdots 5PT$ are 0.70 and 0.73 eV, respectively. The band gap increases with increase in length of oligothiophene in sandwich composites, and it is 0.75 eV in $7PT\cdots C_{54}H_{30}\cdots 7PT$ and remains same for the $9PT\cdots C_{54}H_{30}\cdots 9PT$ composite. However, a comparison of the band gaps of $C_{54}H_{30}\cdots nPT$ and $nPT\cdots C_{54}H_{30}\cdots nPT$ composites reveals that higher concentration of graphene results in lowering of optical band gap and increase in conductivity. The graphene nanoribbon composites show appreciable changes in optical band gap values than graphene nanosheet composites compared to pristine polythiophene band gap. The optical band gap decreases with increase in concentration of graphene and the length of oligothiophene in one-sided composites, while in sandwich composites, the band gap increases due to decrease in graphene concentration. The density of HOMO and LUMO of all graphene sheet and ribbon model composites is mainly spread on graphene (Figure 5) and is consistent in all composite systems (Supporting Information), which supports the decrease in band gap as the concentration of graphene increases.

3.4. UV−Vis Spectroscopy Studies. The TD-DFT approach helps in gaining information about the excitation of electrons from lower to higher energy levels. The UV−vis study is substantial in governing the conductivity and sensitivity through charge transfer and HOMO−LUMO gaps.[72] The UV−vis spectra of $C_{54}H_{30}\cdots nPT$ nanoribbon composites are shown in Figure 6, and the spectra of other configurations are shown in Figures S19−S23 of the
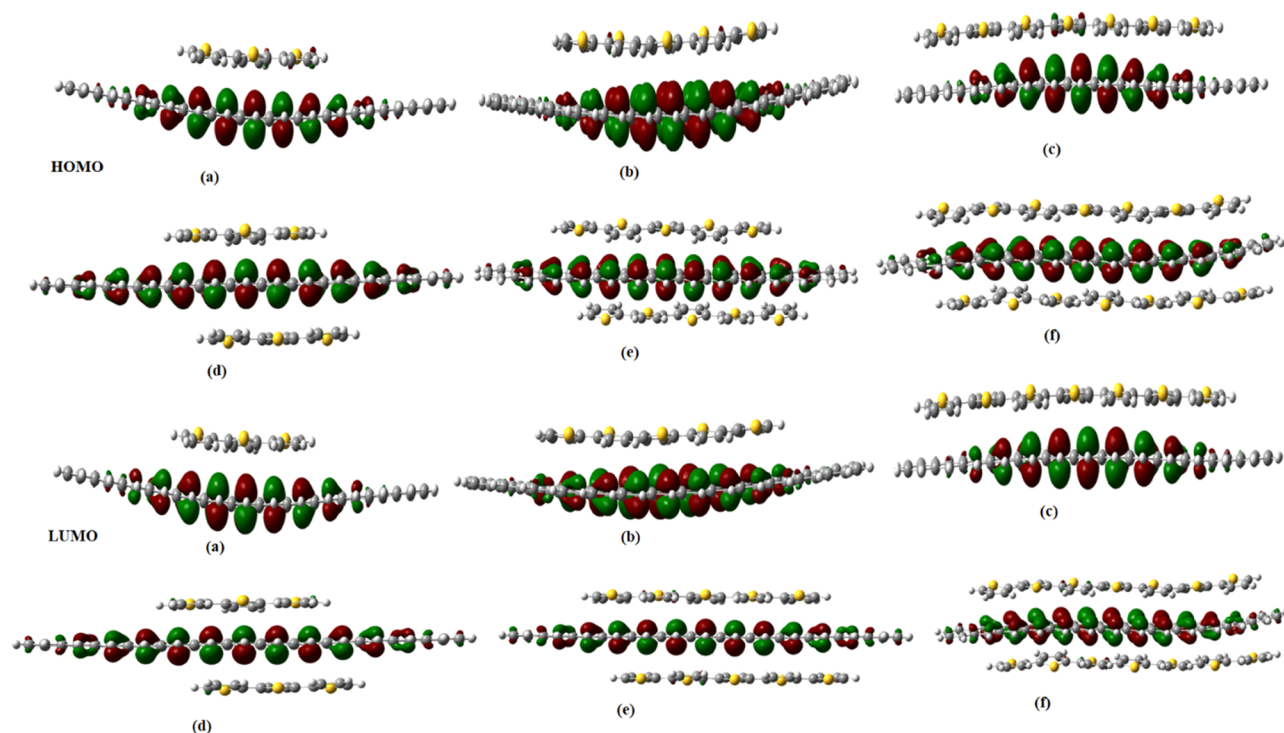
Figure 5. Canonical depiction of HOMO and LUMO orbitals of $nPT\cdots C_{54}H_{30}$ Composite.
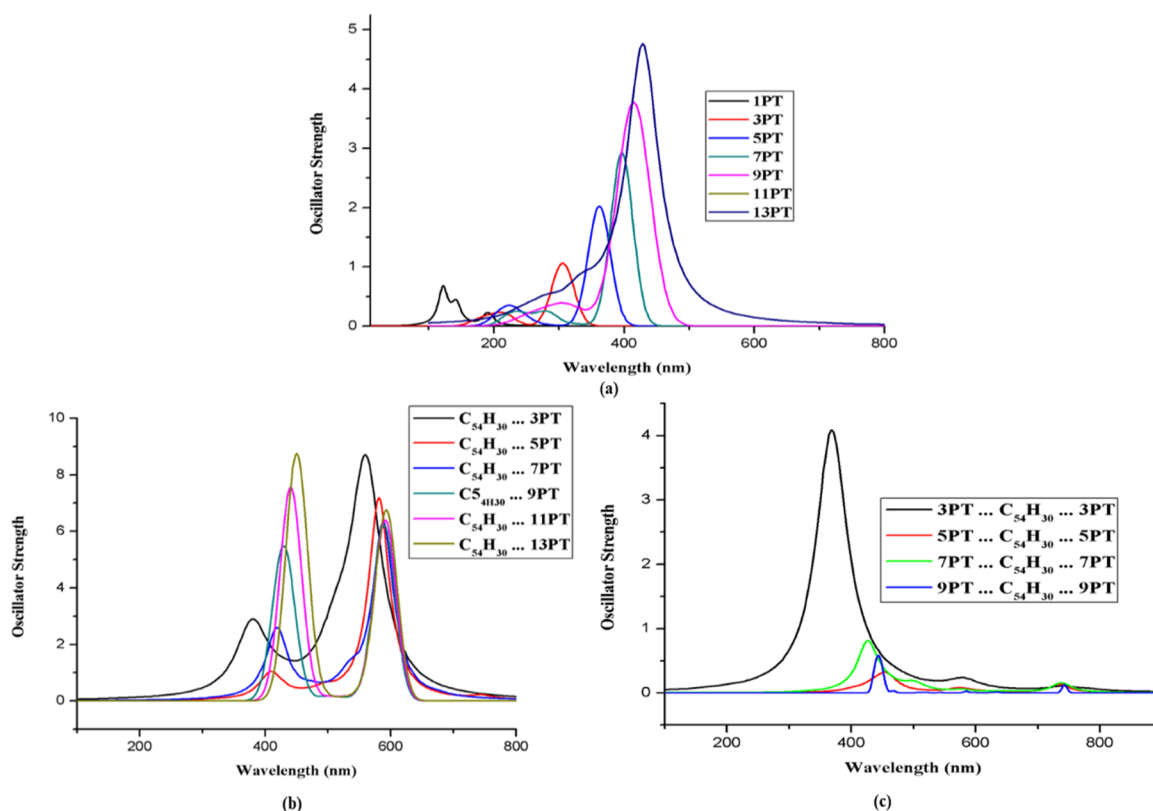
Figure 6. UV−vis spectra of (a) isolated oligothiophene, (b) $C_{54}H_{30}\cdots nPT$, and (c) $nPT\cdots C_{54}H_{30}\cdots nPT$ composites.

Supporting Information. The results of TD-DFT including excitation energies, wavelengths, and oscillator strength of nanosheets composite are listed in Table 2, and those of nanoribbons are listed in Table 3. The λ_{max} of pristine oligothiophene increases due to increase in conjugation as the length of the chain increases. The λ_{max} of 1PT is 123 nm, which increased to 306 nm for 3PT, 361 nm for 5PT, 397 nm for 7PT, and 415 nm for 9PT. The λ_{max} values of 11PT and 13PT are 428 and 433 nm, respectively.

3.4.1. $C_{30}H_{14}\cdots nPT$ Composites. The $C_{30}H_{14}\cdots nPT$ nanosheet composites show a shift in wavelength toward longer region compared to pristine oligothiophene. The λ_{max} of $C_{30}H_{14}\cdots 1PT$ is 420 nm, whereas the λ_{max} values of $C_{30}H_{14}\cdots 3PT$ and $C_{30}H_{14}\cdots 5PT$ are 319 and 375 nm, respectively. The increase in wavelength is due to increase in conjugation after compositing with graphene. This increase in conjugation results in lowering of the energy gap for $\pi-\pi^*$ transition, and the absorbed wavelength shifts to the longer region. The λ_{max} of the $1PT\cdots C_{30}H_{14}\cdots 1PT$ sandwich composite is 427 nm and 319 nm for the $3PT\cdots C_{30}H_{14}\cdots 3PT$ composite. The $5PT\cdots C_{30}H_{14}\cdots 5PT$ composite shows λ_{max} at 418 nm. The wavelength increases compared to one-sided composite as the oligothiophene on both sides of graphene sheet increases the conjugation of π electrons. The increase in conjugation lowers the energy gaps between HOMO and LUMO, and the excitation of electron from HOMO to LUMO requires less energy and wavelength shifted towards the visible region.

3.4.2. $C_{46}H_{18}\cdots nPT$ Composites. The λ_{max} values of $C_{46}H_{18}\cdots 1PT$, $C_{46}H_{18}\cdots 3PT$, and $C_{46}H_{18}\cdots 5PT$ are 320, 311, and 324 nm, respectively. The sandwich composite $1PT\cdots C_{46}H_{18}\cdots 1PT$ exhibits λ_{max} at 320 nm as one-sided $1PT\cdots C_{46}H_{18}$ sheet composite. The $3PT\cdots C_{46}H_{18}\cdots 3PT$ composite shows a significant increase in λ_{max} at 742 nm, and this shifting of

wavelength toward the longer region is due to increase in conjugation and lowers the energy for $\pi-\pi^*$ transition. The λ_{max} of the $5PT\cdots C_{46}H_{18}\cdots 5PT$ composite is 386 nm longer than the corresponding one-sided composite.

3.4.3. $C_{59}H_{20}\cdots nPT$ Composites. The $C_{59}H_{20}\cdots nPT$ sheet composites show λ_{max} closer to the visible region. The λ_{max} of $C_{59}H_{20}\cdots 1PT$ is 389 nm. The wavelength increases to 445 nm for $C_{59}H_{20}\cdots 3PT$ and to 525 nm for $C_{59}H_{20}\cdots 5PT$ composites. The increase in wavelength is due to increase in conjugation of π electrons, and this conjugation decreases the energy gap for $\pi-\pi^*$ transition and the light absorbed in the visible region. The $nPT\cdots C_{59}H_{20}\cdots nPT$ sandwich composites also show a shift in wavelength toward the longer region. The λ_{max} of $1PT\cdots C_{59}H_{20}\cdots 1PT$ is 392 nm and for $3PT\cdots C_{59}H_{20}\cdots 3PT$ is 441 nm. The $5PT\cdots C_{59}H_{20}\cdots 5PT$ composite shows λ_{max} at 579 nm. The oligothiophene on both sides of graphene sheet increases the conjugation and narrows the energy gap for $\pi-\pi^*$ transition and a red shift is observed.

3.4.4. $C_{38}H_{22}\cdots nPT$ Composites. The $C_{38}H_{22}\cdots nPT$ nanoribbon composites also show a shift in wavelength compared to pristine oligothiophene. The λ_{max} of $C_{38}H_{22}\cdots 1PT$ is 314 nm. The UV−vis spectra of $C_{38}H_{22}\cdots 3PT$ and $C_{38}H_{22}\cdots 5PT$ composites are blue-shifted to 304 and 307 nm, respectively, compared to pristine 3PT (306 nm) and 5PT (361 nm). This blue shift is due to less overlap between π orbitals, which decreases the length of conjugation. The absorption maximum increases when the graphene ribbon is loaded with 1PT on both sides. The absorption maximum is increased to 315 nm for $1PT\cdots C_{38}H_{22}\cdots 1PT$. The λ_{max} values of $3PT\cdots C_{38}H_{22}\cdots 3PT$ and $5PT\cdots C_{38}H_{22}\cdots 5PT$ are 317 and 347 nm, respectively. The loading of oligothiophene on both sides increases the overlap between π orbital, which increases the conjugation, and a red shift is observed. The loading of oligothiophene on the larger
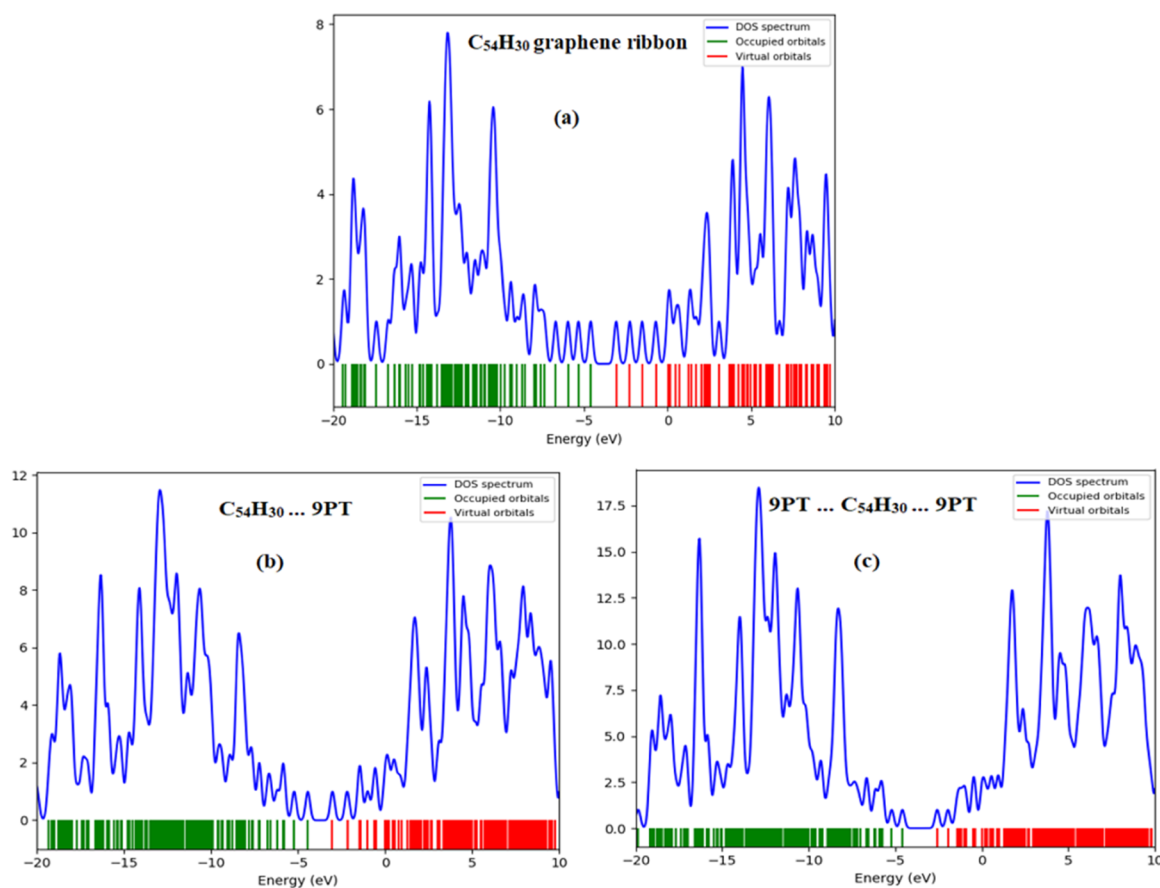
Figure 7. DOS spectrum of (a) $C_{54}H_{30}$, (b) $C_{54}H_{30}\cdots9PT$, and (c) $9PT\cdots C_{54}H_{30}\cdots9PT$ composites.

graphene ribbon in $C_{46}H_{26}\cdots nPT$ increases the wavelength compared to the $C_{38}H_{22}\cdots nPT$ composites.

3.4.5. $C_{46}H_{26}\cdots nPT$ Composites. The λ_{max} of $C_{46}H_{26}\cdots3PT$ is 500 nm. It shifts to the longer wavelength region in $C_{46}H_{26}\cdots5PT$ (at 530 nm) but blue-shifted to 392 nm in $C_{46}H_{26}\cdots7PT$. The blue shift in the 7PT composite is due to less conjugation of π electrons and wavelength spilling to the shorter region. The absorption maximum of sandwich composites of the $C_{46}H_{26}$ graphene nanoribbon shows blue shift as the extent of conjugation decreases between π electrons and the energy gap increases in $3PT\cdots C_{46}H_{26}\cdots3PT$ (360 nm) and $5PT\cdots C_{46}H_{26}\cdots5PT$ (431 nm) composites. The $7PT\cdots C_{46}H_{26}\cdots7PT$ composites show a red shift (λ_{max} at 419 nm compared to 392 nm for $C_{46}H_{26}\cdots7P$).

3.4.6. $C_{54}H_{30}\cdots nPT$ Composites. A further increase in the concentration of graphene in $C_{54}H_{30}\cdots nPT$ nanoribbons has a larger effect on wavelength and peaks are shifted to the longer region. The $C_{54}H_{30}\cdots3PT$ composite shows a peak at 560 nm. A continuous red shift is observed as we load the graphene with increasing units of oligothiophene. The maximum wavelength values of $C_{54}H_{30}\cdots5PT$, $C_{54}H_{30}\cdots7PT$, and $C_{54}H_{30}\cdots9PT$ are 582, 587, and 590 nm, respectively. The $C_{54}H_{30}\cdots11PT$ and $C_{54}H_{30}\cdots13PT$ composites show maximum peaks at 592 and 594 nm, respectively. The larger graphene ribbon shows increase in the electronic conjugation. This increase in the length of conjugation lowers the energy gap for $\pi-\pi^*$ transition, and light are strongly absorbed in the visible region. The two-sided loading of oligothiophene on graphene ribbon causes a blue shift in wavelength. The absorption maxima of $3PT\cdots C_{54}H_{30}\cdots3PT$ and $5PT\cdots C_{54}H_{30}\cdots5PT$ are

368 and 456 nm, respectively. The $7PT\cdots C_{54}H_{30}\cdots7PT$ and $9PT\cdots C_{54}H_{30}\cdots9PT$ composites also show blue shift, and their λ_{max} values are observed at 426 and 446 nm, compared to their one-sided composites at 592 and 594 nm, respectively. The blue shift is due to increase in the energy gap for $\pi-\pi^*$ transition. The increase in energy gap is due to decrease in the concentration of graphene in sandwich complexes.

The UV−vis analysis of all these composites agrees well with the band gap values and binding energies. The UV−vis results of $C_{54}H_{30}\cdots nPT$ nanoribbon composites show a red shift, which strongly coincides with increasing electronic conjugation and narrow band gap. The oscillator strength also has theoretical significance besides λ_{max}. The oscillator strength rises as the interaction increases between species because of the strong overlapping of wave functions.[73] The oscillator strength increases when graphene is composited with oligothiophene, and energies of electronic transitions are shifted toward higher values with increasing conjugation. This significant change in the absorption character of the $C_{54}H_{30}\cdots nPT$ nanoribbon composites can be useful for chemical sensor applications.

3.5. Density of States. The electronic behavior of graphene/polythiophene nanosheet and nanoribbon composites is further confirmed by total density of states (TDOS). The TDOS of pristine graphene ($C_{54}H_{30}$) and $C_{54}H_{30}\cdots9PT$ nanoribbon composites with one-sided oligothiophene and in sandwich configuration is shown in Figure 7a−c. The corresponding plots of other configurations are shown in Figures S24−S29. The DOS spectrum gives us an estimate of the number of energy states at particular energy level that are
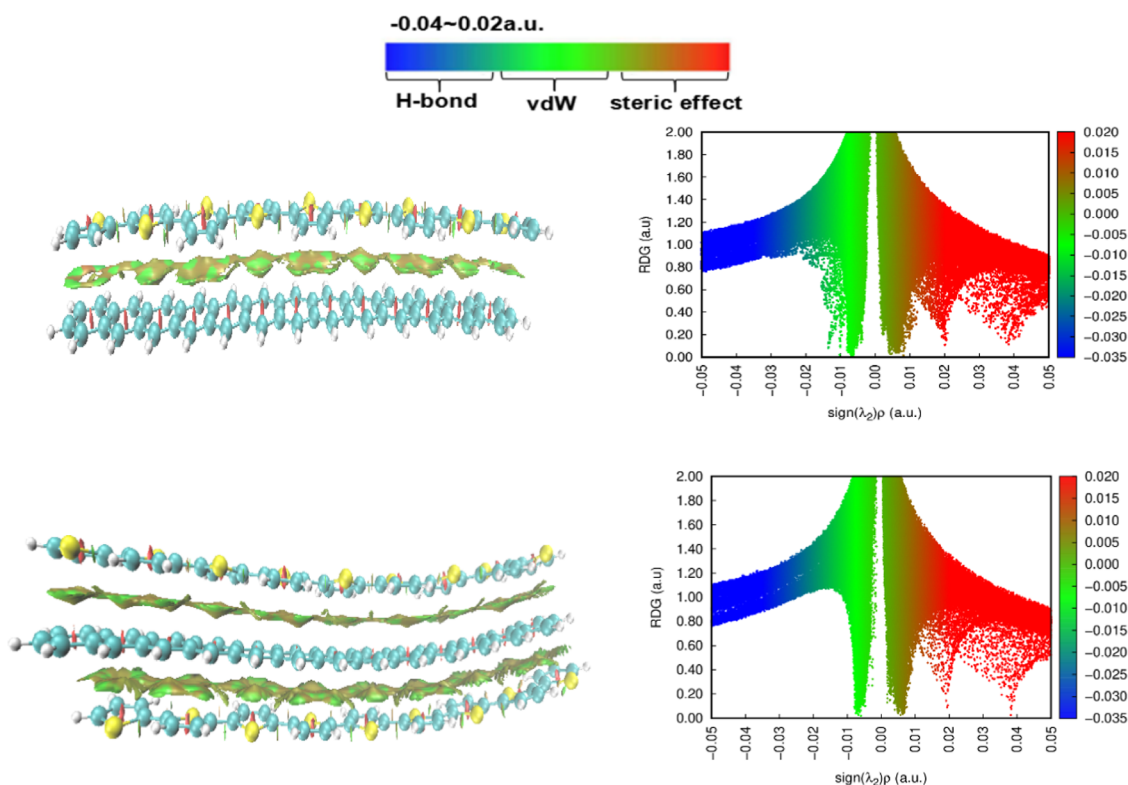
Figure 8. Color-mapped RDG isosurface graphs and scatter diagrams of $C_{54}H_{30}\cdots9PT$ and $9PT\cdots C_{54}H_{30}\cdots9PT$ composites.

available to an electron. The small change that usually occurs in the DOS spectrum in the HOMO and LUMO region has a great influence on the conducting properties of these semiconductor materials. The change in the HOMO and LUMO region is attributed to variation in band gap, which causes change in conductivity. The loading of graphene on polythiophene results new energy levels. The newly generated HOMOs have higher energy compared to pristine oligothiophene HOMOs, which results in the decrease of the HOMO−LUMO gap. The small band gap leads to mobile π electrons and the greater distribution of energy throughout the composite and stabilizing it. This mobility and conjugation of π electrons in these graphene/oligothiophene composites make them good semiconductor materials as energy gap becomes smaller.

3.6. NCI-RDG Analysis. A graphical visualization of the noncovalent interaction regions in real space is obtained by the method of noncovalent interaction analysis to distinguish hydrogen-bond, van der Waals (vdW) interactions, and repulsive steric interactions.[74] NCI plots are generated to probe the existence of weak interactions. The noncovalent interaction index (NCI) uses quantum-mechanical electron density to identify the noncovalent bonds. The reduced density gradient (RDG), which is the derivative of electron density, is defined as

$$RDG(\mathbf{r}) = \frac{1}{2(3\pi^2)^{1/3}} \frac{|\nabla\rho(\mathbf{r})|}{\rho(\mathbf{r})^{4/3}} \qquad (2)$$

NCI plots are generated by plotting reduced density gradient RDG versus $(\text{sign } \lambda_2)\, \rho$. The $(\text{sign } \lambda_2)\, \rho$ is electron density multiplied by the second largest eigenvalue of the Hessian matrix of electron density referred as λ_2. The value of $\rho(\mathbf{r})$ gives the strength of bond, and the function with sign λ_2

expresses the type of bond. The interactions are repulsive if $(\text{sign } \lambda_2)\, \rho > 0$ and attractive if $(\text{sign } \lambda_2)\, \rho < 0$, and for van der Waals type interaction, $(\text{sign } \lambda_2)\, \rho \leq 0$. The color of the isosurface is decided by the value of sign $(\lambda_2)\, \rho$. The color-mapped isosurfaces and their respective scatter plots of reduced density gradient (RDG) versus sign $(\lambda_2)\, \rho$ of $C_{54}H_{30}\cdots9PT$ nanoribbon composite in one-sided and sandwich configurations are shown in Figure 8. The scatter plots and color-mapped surfaces of other composites are shown in Figures S30−S41 of the Supporting Information. The red, green, and blue color codes according to the value of sign $(\lambda_2)\, \rho$ ranging from −0.04 to 0.02 au are used to describe destabilizing steric interactions (0.02−0.04 au), van der Waals (−0.01 to 0.01 au),[75] and stabilizing hydrogen bond (−0.01 to −0.04 au). The color-filled RDG surfaces also indicate the type of interaction according to the color codes. All of the composites show green or light brown color RDG isosurface, indicating the existence of low-gradient, low-density areas of nonbonded overlap. The region in the center of rings is filled by red as they show a strong steric effect. The $\pi\cdots\pi$ stacking interactions are clearly manifested by the isosurfaces filling the interlayer space between graphene and oligothiophene in nanosheets and nanoribbon composites. The noncovalent surface extends as the length of oligothiophene increases to 5PT in $C_{30}H_{14}$, $C_{46}H_{18}$, and $C_{59}H_{20}$ sheet composites (Supporting Information). The ribbon composites also show extension in the RDG surface with increase in length of oligothiophene. The extension of noncovalent surface is up to 5PT in $C_{38}H_{22}$, 7PT in $C_{46}H_{26}$, and 9PT in $C_{54}H_{30}$ graphene ribbon composites. Generally, two spikes are obtained in RDG scatter plots of composites. The green spikes at sign $(\lambda_2)\, \rho$ value −0.01 to 0.01 indicate the vdW interactions, and the red spikes at sign $(\lambda_2)\, \rho$ value 0.02−0.04 au indicate the destabilizing interactions. The green spikes also show the

small displacement in the −0.01 to 0.01 region as the concentration of graphene increases in sheet and ribbon models and when oligothiophene composited with graphene. These colored RDG map surfaces and spikes indicate the existence of noncovalent interaction between oligothiophene and graphene and are in accordance with the results of interaction energies, band gap, UV−vis analysis, and density of states.

4. CONCLUSIONS

Graphene−polythiophene composites have been extensively used in various fields since last several decades; however, theoretical details about the structural and electronic properties are not understood. A proper description of a theoretical model for these composites is quite challenging mainly due to low concentration of graphene in composites. Herein, we present the first detailed theoretical study to unveil the structural, electronic, and optical properties of polythiophene−graphene composites. DFT calculations with the M06-2X method are performed on different models of graphene (nanosheet and nanoribbon) to realize the accurate model for adequately describing the properties of graphene−polythiophene composites. Moreover, the ribbons ($C_{38}H_{22}$, $C_{46}H_{26}$, $C_{54}H_{30}$) and sheets ($C_{30}H_{14}$, $C_{46}H_{18}$, $C_{59}H_{20}$) of different numbers of carbon atoms are considered. Oligothiophenes (nPT) of reasonable length (n = 1−13) are placed on graphene nanosheet, as well as nanoribbon models in different orientations, including vertical, tilted, and π stacking. The calculations reveal that π stacking is the preferred orientation for interaction between oligothiophene and graphene nanosheet. The stability of composites increases as the size of graphene sheet increases from $C_{30}H_{14}$ to $C_{59}H_{20}$. Interaction energies are calculated with M06-2X/6-31G(d), M06-2X-D3/6-31G(d), M06-2X-D3/6-31G(d) (CP), and ωB97M-V/def2-TZVPD (CP) functionals. An accurate estimate of interaction energies is obtained with counterpoise-corrected ωB97M-V(CP)/def2-TZVPD. The interaction energy increases from −8.64 kcal mol^{-1} in $C_{30}H_{14}\cdots$1PT to −41.79 kcal mol^{-1} in $C_{59}H_{20}\cdots$5PT sheet composites. The sandwich complexes of oligothiophene and graphene nanosheet also show an increase in interaction energy from −17.46 kcal mol^{-1} in 1PT$\cdots$$C_{30}H_{14}\cdots$1PT to −85.07 kcal mol^{-1} in 5PT$\cdots$$C_{59}H_{20}\cdots$5PT composites. The interaction energy for nanoribbons ranges from −6.75 kcal mol^{-1} in $C_{38}H_{22}\cdots$1PT to −55.65 kcal mol^{-1} in $C_{54}H_{30}\cdots$13PT composites. The sandwich composites of oligothiophene and graphene nanoribbon show increase in interaction energy from −13.74 kcal mol^{-1} in 1PT$\cdots$$C_{38}H_{22}\cdots$1PT to −135.40 kcal mol^{-1} in 9PT$\cdots$$C_{54}H_{30}\cdots$9PT composites. The ribbon models of graphene−polythiophene composites show higher interaction energies than the sheet models of graphene−polythiophene. The interaction energies between oligothiophene and graphene model are as high as −193.02 kcal mol^{-1} for graphene ribbon. The nature and strength of interaction are evaluated through interaction energies and NCI plots. Many of these composites show superadditivity of interaction energies. The superadditivity of interaction energies is more pronounced for the graphene nanoribbon model than the graphene nanosheet model. The NCI plots reveal the visualization of regions where noncovalent interactions occur in real space and distinguish the hydrogen-bond, van der Waals, and repulsive steric interactions. Frontier molecular orbital analysis reveals a significant decrease in the band gap. The optical band gap decreases by increasing the concentration

of graphene, and it is improved when the proportion of graphene is increased by using $C_{46}H_{26}$ and $C_{54}H_{30}$ larger nanoribbons. The density of states analysis is performed to explore the electronic properties and to further support the inferences obtained from molecular orbital analysis.

■ ASSOCIATED CONTENT

ⓈSupporting Information

The Supporting Information is available free of charge at https://pubs.acs.org/doi/10.1021/acs.jpcc.9b08090.

> Optimized configurations of all sheets and ribbon models; a plot of basis set comparison of different methods; calculation table for D3 correction; canonical depiction of all sheets and ribbon models; UV−vis spectra; DOS plots; and color-mapped isosurfaces and scatter diagrams (PDF)

■ AUTHOR INFORMATION

Corresponding Author
*E-mail: khurshid@cuiatd.edu.pk. Phone: +92-992-383591-6. Fax: +92-992-383441.

ORCID ⓞ
Kevin Carter-Fenk: 0000-0001-8302-4750
John M. Herbert: 0000-0002-1663-2278
Khurshid Ayub: 0000-0003-0990-1860

Notes
The authors declare no competing financial interest.

■ REFERENCES

(1) Ritter, K. A.; Lyding, J. W. The Influence of Edge Structure on the Electronic Properties of Graphene Quantum Dots and Nanoribbons. *Nat. Mater.* **2009**, *8*, 235−242.

(2) Dai, L. Functionalization of Graphene for Efficient Energy Conversion and Storage. *Acc. Chem. Res.* **2013**, *46*, 31−42.

(3) Zhang, Z.; Luo, L.; Chen, G.; Ding, Y.; Deng, D.; Fan, C. Tryptamine Functionalized Reduced Graphene Oxide for Label-Free DNA Impedimetric Biosensing. *Biosens. Bioelectron.* **2014**, *60*, 161−166.

(4) Weaver, C. L.; Larosa, J. M.; Luo, X.; Cui, X. T. Electrically Controlled Drug Delivery from Graphene Oxide Nanocomposite Films. *ACS Nano* **2014**, *8*, 1834−1843.

(5) Huang, W.; Hao, Q.; Lei, W.; Wu, L.; Xia, X. Polypyrrole-Hemin-Reduce Graphene Oxide: Rapid Synthesis and Enhanced Electrocatalytic Activity towards the Reduction of Hydrogen Peroxide. *Mater. Res. Express* **2015**, *1*, No. 045601.

(6) Katsnelson, M. I.; Novoselov, K. S. Graphene: New Bridge between Condensed Matter Physics and Quantum Electrodynamics. *Solid State Commun.* **2007**, 3.

(7) Georgakilas, V.; Otyepka, M.; Bourlinos, A. B.; Chandra, V.; Kim, N.; Kemp, K. C.; Hobza, P.; Zboril, R.; Kim, K. S.

Functionalization of Graphene: Covalent and Non-Covalent Approaches, Derivatives and Applications. *Chem. Rev.* **2012**, *112*, 6156−6214.

(8) Lonkar, S. P.; Deshmukh, Y. S.; Abdala, A. A. Recent Advances in Chemical Modifications of Graphene. *Nano Res.* **2015**, 1039−1074.

(9) Wang, Q. H.; Hersam, M. C. Room-Temperature Molecular-Resolution Characterization of Self-Assembled Organic Monolayers on Epitaxial Graphene. *Nat. Chem.* **2009**, *1*, 206−211.

(10) Si, Y.; Samulski, E. T. Synthesis of Water Soluble Graphene. *Nano Lett.* **2008**, *8*, 1679−1682.

(11) Bostwick, A.; Ohta, T.; Seyller, T.; Horn, K.; Rotenberg, E. Quasiparticle Dynamics in Graphene. *Nat. Phys.* **2007**, *3*, 36−40.

(12) Kim, K. S.; Zhao, Y.; Jang, H.; Lee, S. Y.; Kim, J. M.; Kim, K. S.; Ahn, J.-H.; Kim, P.; Choi, J.-Y.; Hong, B. H. Large-Scale Pattern Growth of Graphene Films for Stretchable Transparent Electrodes. *Nature* **2009**, *457*, 706−710.

(13) Lee, Y.; Bae, S.; Jang, H.; Jang, S.; Zhu, S. E.; Sim, S. H.; Song, Y., Il; Hong, B. H.; Ahn, J. H. Wafer-Scale Synthesis and Transfer of Graphene Films. *Nano Lett.* **2010**, *10*, 490−493.

(14) Wang, G.; Yang, J.; Park, J.; Gou, X.; Wang, B.; Liu, H.; Yao, J. Facile Synthesis and Characterization of Graphene Nanosheets. *J. Phys. Chem. C* **2008**, *112*, 8192−8195.

(15) Zhu, C.; Guo, S.; Fang, Y.; Dong, S. Reducing Sugar: New Functional Molecules for the Green Synthesis of Graphene Nanosheets. *ACS Nano* **2010**, *4*, 2429−2437.

(16) Fan, Z.-J.; Kai, W.; Yan, J.; Wei, T.; Zhi, L.-J.; Feng, J.; Ren, Y.-m.; Song, L.-P.; Wei, F. Facile Synthesis of Graphene Nanosheets via Fe Reduction of Exfoliated Graphite Oxide. *ACS Nano* **2010**, *5*, 191−198.

(17) Chen, H.; Müller, M. B.; Gilmore, K. J.; Wallace, G. G.; Li, D. Mechanically Strong, Electrically Conductive, and Biocompatible Graphene Paper. *Adv. Mater.* **2008**, *20*, 3557−3561.

(18) Zhang, L.; Dai, H.; Lee, S.; Wang, X.; Li, X. Chemically Derived, Ultrasmooth Graphene Nanoribbon Semiconductors. *Science* **2008**, *319*, 1229−1232.

(19) Jiao, L.; Zhang, L.; Wang, X.; Diankov, G.; Dai, H. Narrow Graphene Nanoribbons from Carbon Nanotubes. *Nature* **2009**, *458*, 877.

(20) Huang, X.; Qian, K.; Yang, J.; Zhang, J.; Li, L.; Yu, C.; Zhao, D. Functional Nanoporous Graphene Foams with Controlled Pore Sizes. *Adv. Mater.* **2012**, *24*, 4419−4423.

(21) Chen, Z.; Xu, C.; Ma, C.; Ren, W.; Cheng, H. M. Lightweight and Flexible Graphene Foam Composites for High-Performance Electromagnetic Interference Shielding. *Adv. Mater.* **2013**, *25*, 1296−1300.

(22) Chowdhury, S.; Bandyopadhyay, A.; Dhar, N.; Jana, D. Optical and Magnetic Properties of Free-Standing Silicene, Germanene and T-Graphene System. *Phys. Sci. Rev.* **2018**, *2*, 2365−6581.

(23) Li, L. S.; Yan, X. Colloidal Graphene Quantum Dots. *J. Phys. Chem. Lett.* **2010**, *1*, 2572−2576.

(24) Bandyopadhyay, A.; Nandy, A.; Chakrabarti, A.; Jana, D. Optical Properties and Magnetic Flux-Induced Electronic Band Tuning of a T-Graphene Sheet and Nanoribbon. *Phys. Chem. Chem. Phys.* **2017**, *19*, 21584−21594.

(25) Park, J.; Jo, S. B.; Yu, Y. J.; Kim, Y.; Yang, J. W.; Lee, W. H.; Kim, H. H.; Hong, B. H.; Kim, P.; Cho, K.; et al. Single-Gate Bandgap Opening of Bilayer Graphene by Dual Molecular Doping. *Adv. Mater.* **2012**, *24*, 407−411.

(26) Sun, H.; Wu, L.; Wei, W.; Qu, X. Recent Advances in Graphene Quantum Dots for Sensing. *Mater. Today* **2013**, 433−442.

(27) Das, R.; Dhar, N.; Bandyopadhyay, A.; Jana, D. Size Dependent Magnetic and Optical Properties in Diamond Shaped Graphene Quantum Dots: A DFT Study. *J. Phys. Chem. Solids* **2016**, *99*, 34−42.

(28) Zhang, Z.; Huang, H.; Yang, X.; Zang, L. Tailoring Electronic Properties of Graphene by π-π Stacking with Aromatic Molecules. *J. Phys. Chem. Lett.* **2011**, 2897−2905.

(29) Kim, I. H.; Jeong, Y. G. Polylactide/Exfoliated Graphite Nanocomposites with Enhanced Thermal Stability, Mechanical

(30) Yu, A.; Ramesh, P.; Itkis, M. E.; Bekyarova, E.; Haddon, R. C. Graphite Nanoplatelet-Epoxy Composite Thermal Interface Materials. *J. Phys. Chem. C* **2007**, *111*, 7565−7569.

(31) Ramanathan, T.; Abdala, A. A.; Stankovich, S.; Dikin, D. A.; Herrera-Alonso, M.; Piner, R. D.; Adamson, D. H.; Schniepp, H. C.; Chen, X.; Ruoff, R. S.; et al. Functionalized Graphene Sheets for Polymer Nanocomposites. *Nat. Nanotechnol.* **2008**, *3*, 327−331.

(32) Wohner, N.; Lam, P.; Sattler, K. Energetic Stability of Graphene Nanoflakes and Nanocones. *Carbon* **2014**, *67*, 721−735.

(33) Hu, Y.; Bao, C. L.; Guo, Y. Q.; Song, L. Poly(Vinyl Alcohol) Nanocomposites Based on Graphene and Graphite Oxide: A Comparative Investigation of Property and Mechanism. *J. Mater. Chem.* **2011**, *21*, 13942−13950.

(34) Kuila, T.; Sheng, Y. D.; Murmu, N. C. Graphene/Conjugated Polymer Nanocomposites for Optoelectronic and Biological Applications. *Fundam. Conjugated Polym. Blends, Copolym. Compos.* **2015**, 229−279.

(35) Li, Y.; Huang, Y.; Qi, S.; Niu, L.; Zhang, Y.; Wu, Y. Preparation, Magnetic and Electromagnetic Properties of Polyaniline/Strontium Ferrite/Multiwalled Carbon Nanotubes Composite. *Appl. Surf. Sci.* **2012**, *258*, 3659−3666.

(36) Wang, Y.; Huang, Y.; Wang, Q.; He, Q.; Chen, L. Preparation and Electromagnetic Properties of Polyaniline(Polypyrrole)-BaFe12O19/Ni0.8Zn0.2Fe2O4 Ferrite Nanocomposites. *Appl. Surf. Sci.* **2012**, *259*, 486−493.

(37) Hsieh, T. H.; Ho, K. S.; Bi, X.; Huang, C. H.; Wang, Y. Z.; Han, Y. K.; Chen, Z. L.; Hsu, C. H.; Li, P. H.; Chang, Y. C. Effects of [SDS]/[H 2 O] Molar Ratio on the Electromagnetic Properties of Polyaniline/Maghemite Nanocomposites. *Synth. Met.* **2010**, *160*, 1609−1616.

(38) Moon, Y. E.; Yun, J.; Kim, H., Il. Synergetic Improvement in Electromagnetic Interference Shielding Characteristics of Polyaniline-Coated Graphite Oxide/γ-Fe$_2$O$_3$/BaTiO$_3$ Nanocomposites. *J. Ind. Eng. Chem.* **2013**, *19*, 493−497.

(39) Cogal, S.; Calio, L.; Celik Cogal, G.; Salado, M.; Kazim, S.; Oksuz, L.; Ahmad, S.; Uygun Oksuz, A. RF Plasma-Enhanced Graphene−Polymer Composites as Hole Transport Materials for Perovskite Solar Cells. *Polym. Bull.* **2018**, *75*, 4531−4545.

(40) Zhao, J.; Xie, Y.; Le, Z.; Yu, J.; Gao, Y.; Zhong, R.; Qin, Y.; Huang, Y. Preparation and Characterization of an Electromagnetic Material: The Graphene Nanosheet/Polythiophene Composite. *Synth. Met.* **2013**, *181*, 110−116.

(41) Iguchi, H.; Miyahara, K.; Higashi, C.; Fujita, K.; Nakagawa, N.; Tamba, S.; Mori, A.; Yoshitani, H.; Nakasuga, A.; Maruyama, T. Preparation of Uncurled and Planar Multilayered Graphene Using Polythiophene Derivatives via Liquid-Phase Exfoliation of Graphite. *FlatChem* **2018**, *8*, 31−39.

(42) Abdelkarim, R. B.; Yahiaoui, A.; Hachemaoui, A.; Belbachir, M.; Khelil, A. Synthesis and Properties of PolythiophèNe Benzylidene and Their Photovoltaic Applications. *Mater. Sci. Appl.* **2011**, *02*, 1014−1021.

(43) Nayebi, P.; Zaminpayma, E. A Molecular Dynamic Simulation Study of Mechanical Properties of Graphene-Polythiophene Composite with Reax Force Field. *Phys. Lett. A* **2016**, *380*, 628−633.

(44) Mombrú, D.; Romero, M.; Faccio, R.; Mombrú, ÁW. Electronic Structure of Edge-Modified Graphene Quantum Dots Interacting with Polyaniline: Vibrational and Optical Properties. *J. Phys. Chem. C* **2017**, *121*, 16576−16583.

(45) Shao, Y.; Gan, Z.; Epifanovsky, E.; Gilbert, A. T. B.; Wormit, M.; Kussmann, J.; Lange, A. W.; Behn, A.; Deng, J.; Feng, X.; et al. Advances in Molecular Quantum Chemistry Contained in the Q-Chem 4 Program Package. *Mol. Phys.* **2015**, *113*, 184−215.

(46) Dennington, R.; Keith, T.; Millam, J. *GaussView*, version 5.0.8; Semichem Inc.: Shawnee Mission, KS, 2009.

(47) IQmol. www.iqmol.org.

(48) Grimme, S. Density Functional Theory with London Dispersion Corrections. *Wiley Interdiscip. Rev.: Comput. Mol. Sci.* **2011**, *1*, 211−228.

(49) Grimme, S.; Hansen, A.; Brandenburg, J. G.; Bannwarth, C. Dispersion-Corrected Mean-Field Electronic Structure Methods. *Chem. Rev.* **2016**, *116*, 5105−5154.

(50) Mardirossian, N.; Head-Gordon, M. How Accurate Are the Minnesota Density Functionals for Noncovalent Interactions, Isomerization Energies, Thermochemistry, and Barrier Heights Involving Molecules Composed of Main-Group Elements? *J. Chem. Theory Comput.* **2016**, *12*, 4303−4325.

(51) Mardirossian, N.; Head-Gordon, M. ω B97M-V: A Combinatorially Optimized, Range-Separated Hybrid, Meta-GGA Density Functional with VV10 Nonlocal Correlation. *J. Chem. Phys.* **2016**, *144*, No. 214110.

(52) Hohenstein, E. G.; Chill, S. T.; Sherrill, C. D. Assessment of the Performance of the M05-2X and M06-2X Exchange-Correlation Functionals for Noncovalent Interactions in Biomolecules. *J. Chem. Theory Comput.* **2008**, *4*, 1996−2000.

(53) Zhao, Y.; Truhlar, D. G. The M06 Suite of Density Functionals for Main Group Thermochemistry, Thermochemical Kinetics, Noncovalent Interactions, Excited States, and Transition Elements: Two New Functionals and Systematic Testing of Four M06-Class Functionals and 12 Other Function. *Theor. Chem. Acc.* **2008**, *120*, 215−241.

(54) Suvitha, A.; Venkataramanan, N. S. Trapping of Organophosphorus Chemical Nerve Agents by Pillar[5]Arene: A DFT, AIM, NCI and EDA Analysis. *J. Inclusion Phenom. Macrocyclic Chem.* **2017**, *87*, 207−218.

(55) Zade, S. S.; Bendikov, M. From Oligomers to Polymer: Convergence in the HOMO-LUMO Gaps of Conjugated Oligomers. *Org. Lett.* **2006**, *8*, 5243−5246.

(56) Ullah, H.; Shah, A. U. H. A.; Bilal, S.; Ayub, K. DFT Study of Polyaniline NH3, CO2, and CO Gas Sensors: Comparison with Recent Experimental Data. *J. Phys. Chem. C* **2013**, *117*, 23701−23711.

(57) Wasim, F.; Mahmood, T.; Ayub, K. An Accurate Cost Effective DFT Approach to Study the Sensing Behaviour of Polypyrrole towards Nitrate Ions in Gas and Aqueous Phases. *Phys. Chem. Chem. Phys.* **2016**, *18*, 19236−19247.

(58) Bibi, S.; Ullah, H.; Ahmad, S. M.; Ali Shah, A. U. H.; Bilal, S.; Tahir, A. A.; Ayub, K. Molecular and Electronic Structure Elucidation of Polypyrrole Gas Sensors. *J. Phys. Chem. C* **2015**, *119*, 15994−16003.

(59) Ullah, H.; Shah, A. U. H. A.; Bilal, S.; Ayub, K. Doping and Dedoping Processes of Polypyrrole: DFT Study with Hybrid Functionals. *J. Phys. Chem. C* **2014**, *118*, 17819−17830.

(60) Ahmad, S. M.; Bibi, S.; Bilal, S.; Shah, A. U. H. A.; Ayub, K. Spectral and Electronic Properties of π-Conjugated Oligomers and Polymers of Poly(o-Chloroaniline-Co-o-Toluidine) Calculated with Density Functional Theory. *Synth. Met.* **2015**, *205*, 153−163.

(61) O'boyle, N. M.; Tenderholt, A. L.; Langner, K. M. cclib: A library for package-independent computational chemistry algorithms. *J. Comput. Chem* **2008**, *29*, 839.

(62) Lu, T.; Chen, F. Multiwfn: A Multifunctional Wavefunction Analyzer. *J. Comput. Chem.* **2012**, *33*, 580−592.

(63) Humphrey, W.; Dalke, A.; Schulten, K. VMD: Visual Molecular Dynamics. *J. Mol. Graphics* **1996**, 33−38.

(64) Bora, C.; Sarkar, C.; Mohan, K. J.; Dolui, S. Polythiophene/Graphene Composite as a Highly Efficient Platinum-Free Counter Electrode in Dye-Sensitized Solar Cells. *Electrochim. Acta* **2015**, *157*, 225−231.

(65) Melo, J. P.; Schulz, E. N.; Morales-Verdejo, C.; Horswell, S. L.; Camarada, M. B. Synthesis and Characterization of Graphene/Polythiophene (GR/PT) Nanocomposites: Evaluation as High-Performance Supercapacitor Electrodes. *Int. J. Electrochem. Sci.* **2017**, *12*, 2933−2948.

(66) Liu, K. Y.; Liu, J.; Herbert, J. M. Accuracy of Finite-Difference Harmonic Frequencies in Density Functional Theory. *J. Comput. Chem.* **2017**, *38*, 1678−1684.

(67) Nishio, M. CH/π−Hydrogen Bonds in Crystals. *CrystEngComm* **2004**, *6*, 130−158.

(68) Cheney, B. V.; Schulz, M. W.; Cheney, J. Complexes of Benzene with Formamide and Methanethiol as Models for Interactions of Protein Substructures. *Biochim. Biophys. Acta, Protein Struct. Mol. Enzymol.* **1989**, *996*, 116−124.

(69) Ibáñez-Marín, F.; Morales-Verdejo, C.; Camarada, M. B. Composites of Electrochemically Reduced Graphene Oxide and Polythiophene and Their Application in Supercapacitors. *Int. J. Electrochem. Sci.* **2017**, *12*, 11546−11555.

(70) Bora, C.; Pegu, R.; Saikia, B. J.; Dolui, S. K. Synthesis of Polythiophene/Graphene Oxide Composites by Interfacial Polymerization and Evaluation of Their Electrical and Electrochemical Properties. *Polym. Int.* **2014**, *63*, 2061−2067.

(71) Brédas, J. L. Relationship between Band Gap and Bond Length Alternation in Organic Conjugated Polymers. *J. Chem. Phys.* **1985**, *82*, 3808−3811.

(72) Dishi, O.; Gidron, O. Macrocyclic Oligofurans: A Computational Study. *J. Org. Chem.* **2018**, *83*, 3119−3125.

(73) Vossmeyer, T.; Katsikas, L.; Giersig, M.; Popovic, I. G.; Diesner, K.; Chemseddine, A.; Eychmüller, A.; Weller, H. CdS Nanoclusters: Synthesis, Characterization, Size Dependent Oscillator Strength, Temperature Shift of the Excitonic Transition Energy, and Reversible Absorbance Shift. *J. Phys. Chem. A* **1994**, *98*, 7665−7673.

(74) Venkataramanan, N. S.; Suvitha, A. Journal of Molecular Graphics and Modelling Nature of Bonding and Cooperativity in Linear DMSO Clusters: A DFT, AIM and NCI Analysis. *J. Mol. Graphics Modell.* **2018**, *81*, 50−59.

(75) Wu, Q.; Su, H.; Wang, H.; Wang, H. Ab Initio Calculations, Structure, NBO and NCI Analyses of X−H···Π Interactions. *Chem. Phys. Lett.* **2018**, *693*, 202−209.

(76) Ohio Supercomputer Center. http://osc.edu/ark:/19495/f5s1ph73.